Journal of Materials Chemistry B

ROYAL SOCIETY OF CHEMISTRY

REVIEW

View Article Online
View Journal

Cite this: DOI: 10.1039/d5tb02566d

Imidazolinone-based fluorophores: from green fluorescent proteins to confinement strategies and bioinspired materials design

Sifan Ji,†[a] Sébastien Lecommandoux,[a] Colin Bonduelle *[a] and Chloé Grazon *[b]

Received 19th November 2025,
Accepted 22nd March 2026

DOI: 10.1039/d5tb02566d

rsc.li/materials-b

Fluorescent proteins, such as the green fluorescent protein (GFP) discovered in *Aequorea victoria*, have revolutionized biological researches. Their fluorescence is primarily governed by a dye containing an imidazolinone motif that is buried within the protein core, as well as by its stabilization by the surrounding protein scaffold. Inspired by this structure–property relationship, researchers have developed synthetic imidazolinone-based dyes and engineered confined environments that emulate the folded protein cage. These complementary strategies overcome key limitations of the isolated natural dyes, including low brightness and quenching *via* twisted intramolecular charge transfer (TICT). This review examines the structural and photophysical properties of unnatural imidazolinone-based dyes, as well as the role of confinement in modulating their fluorescence. We compare covalent and non-covalent confinement approaches, highlighting their effects on brightness, stability, and functional versatility. Finally, we discuss emerging applications in imaging, sensing, photocatalysis, phototherapy, and optical devices. We also outline the challenges and opportunities of advancing confined imidazolinone fluorophores beyond natural protein frameworks.

1. Introduction

Fluorescent proteins are a fascinating class of biomacromolecules whose versatility and range of applications have expanded significantly since their discovery in the last century.[1] The history of this class of proteins began with the identification of green fluorescent protein (GFP) from *Aequorea victoria*, as reported by Shimomura in 1962.[2] Intrigued by its emissive properties, Chalfie pioneered the use of GFP as a marker to track gene expression and protein localization in living cells.[3] This groundbreaking discovery significantly advanced biology by providing GFP as a powerful tool to observe living organisms under a microscope. Furthermore, Tsien and coworkers extended the color profile of fluorescent proteins from green to red.[4] In 2008, Shimomura, Chalfie, and Tsien received the Nobel Prize in Chemistry for their work on GFP and its related recombinant proteins, which have become indispensable biotechnological tools across the life science.

The fluorescent proteins possess a comparable three-dimensional structure containing an imidazolinone-based fluorophore, covalently linked to a helical polypeptide and encapsulated within a β-barrel protein scaffold.[5–7] To mimic this fluorescence, a range of synthetic approaches have been developed to access imidazolinone-based dyes, wherein their photophysical properties are finely modulated through structural variations at the R_1, R_2, and R_3 positions (Fig. 1).[8,9] However, most chemically synthesized imidazolinone dyes suffer from limited brightness, mainly due to twisted intramolecular charge transfer (TICT) effects.[10] To overcome this challenge, strategies inspired by the confined environments of folded protein cages have been employed. These approaches exploit non-covalent and covalent interactions to constrain the dyes, effectively suppressing non-radiative energy dissipation and enhancing fluorescence emission by stabilizing dye conformations sensitive to local environmental changes. Following this approach, GFP-like systems have found broad applications across imaging, sensing, photocatalysis, photodynamic therapy, and optical devices (Fig. 1).[11,12]

In this review, we highlight fluorescent and luminescent materials inspired by GFP, focusing on synthetic imidazolinone-based dyes and how confinement in matrices such as polymers, proteins, DNA/RNA, or porous frameworks enhances their brightness and stability (Table 1). We specifically highlight advances in synthesis,

[a] Univ. Bordeaux, CNRS, Bordeaux INP, LCPO, UMR 5629, Pessac, F-33600, France. E-mail: colin.bonduelle@enscbp.fr
[b] Univ. Bordeaux, CNRS, Bordeaux INP, ISM, UMR 5255, Talence, F-33400, France. E-mail: chloe.grazon@u-bordeaux.fr
† Current address: Institute of Zhejiang University-Quzhou, 99 Zheda Road, Quzhou 324000, China.

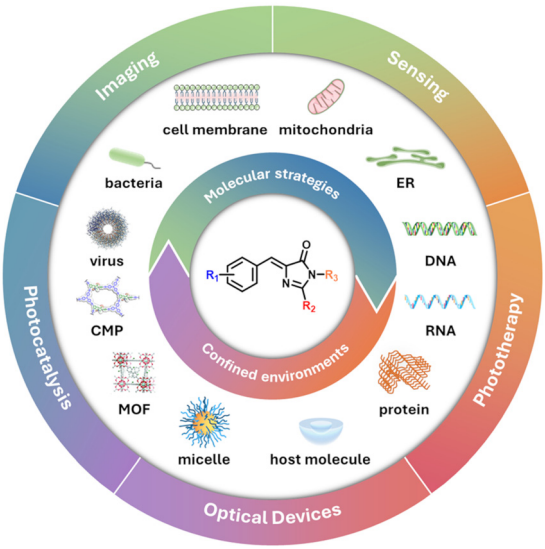

Fig. 1 Examples of confined environments designed to stabilize imidazolinone-based fluorophores, enabling applications in imaging, sensing, and beyond.

strategies to tune photophysical properties, and applications in imaging and sensing, while outlining challenges such as low quantum yields and limited red-shifted emission compared to natural fluorescent proteins.

2. GFP and other fluorescent proteins

The chemical structure of the green fluorescent protein chromophore was first proposed by Shimomura in 1979[13] and later confirmed by Ward in 1993.[14] The chromophore is post-translationally formed through an autocatalytic maturation process involving folding, cyclization, oxidation, and dehydration of the Ser65–Tyr66–Gly67 tripeptide motif on the central polypeptide helix (Fig. 2a).[15,16] The resulting chromophore comprises 4-hydroxybenzylidene-2,3-dimethylimidazolinone (*p*-HBDI) exhibit a push–pull electronic character, in which the imidazolinone ring acts as an electron acceptor and a phenolate moiety behaves as the donor. The full crystal structure of wild-type GFP, derived from *Aequorea victoria* and consisting of 238 amino acid residues, was resolved in 1996 by Tsien and co-workers.[5] These studies revealed that GFP adopts a well-folded β-barrel architecture, composed of eleven β-strands that enclose a central α-helix, within which the chromophore is embedded and protected from the external environment. The GFP β-barrel has a diameter of approximately 2.4 nm and a height of 4.2 nm.[5] This cage-like structure stabilizes the chromophore through an extensive network of hydrogen bonds involving adjacent amino acid residues and structured water molecules.

The native GFP displays two distinct absorption bands at ~380 nm and ~480 nm, corresponding respectively to the neutral and anionic forms of the chromophore(Fig. 2b),[17] the phenolate (Tyr) having a pK_a *ca.* 8 in the *p*-HBDI.[18–20] Upon excitation of the neutral form, the chromophore undergoes excited-state proton transfer (ESPT),[21] in which the proton from the phenolic group is transferred to Glu222 (E222), resulting in an anionic excited-state species that emits green fluorescence (~510 nm) with a fluorescence quantum yield (Φ_f) of 0.7–0.8.[22] Outside the protective β-barrel, the isolated GFP chromophore (*p*-HBDI) is non-fluorescent in solution at both neutral and anionic forms. This diminished emission is due to ultrafast nonradiative decay pathways facilitated by free bond rotation.[23,24] Twisting around either the C=C double bond (one-bond flip) or the adjacent aromatic single bond leads to *cis–trans* isomerization and internal conversion (Fig. 2c).[24,25] A "hula-twist" mechanism, combining these torsional motions (τ and φ), has also been proposed (Fig. 2d).[6,26] In solution, such excited-state twisting results in rapid deactivation (< 1 ps), converting the fluorescent *cis* (*Z*) isomer into a non-emissive *trans* (*E*) form. By contrast, within the rigid β-barrel, these torsional motions are strongly restricted. The structured environment not only inhibits nonradiative decay but also promotes ESPT to E222, enabling efficient fluorescence from the anionic form of *p*-HBDI.[4,5] Thus, the β-barrel plays a critical role in fluorescence activation through both steric confinement and precise electrostatic interactions.

Since the elucidation of GFP structure and function, a broad range of fluorescent protein variants has been discovered and engineered, giving rise to chromophores with emission profiles spanning from blue to red (Fig. 3).[6,27] Despite their spectral diversity, all these proteins contain a β-barrel, with differences arising from slight variations in the chromophore structure and its local environment.[13] Tsien and colleagues engineered blue fluorescent proteins (BFP) by mutating Tyr66 of wild-type GFP to histidine (Y66H), producing blue emission at 448 nm upon UV excitation at 382 nm.[15,28] Similarly, the Y66W mutant (CFP) emits cyan fluorescence (434/477 nm).[15] To shift emission further, yellow fluorescent protein (YFP, λ_{em} = 529 nm) was developed *via* the T203Y mutation by introducing π–π stacking between Tyr203 and Tyr66.[5,29] Red fluorescent proteins (RFPs), such as DsRed from *Discosoma striata*, extend the π-system of the Gln66–Tyr67–Gly68 chromophore through an additional oxidation step, resulting in excitation/emission wavelengths at 557/592 nm.[30] These engineered fluorescent proteins broaden the spectral palette for bioimaging and biosensing applications.[7,31,32] Overall, these studies demonstrated the strong influence of the chemical structure of chromophores and their spatially neighboring residues on structure-dependent fluorescence properties. This elucidation and understanding of the structure–property relationship has fundamentally driven the development of artificial GFP-like systems.

3. Bioinspired imidazolinone-based fluorophores

As previously stated, all members of the GFP family include a comparable chromophore based on the imidazolinone heterocycle, which has been demonstrated to possess notable versatility in these protein systems.[33] In this section, we focus on the

Table 1 Photophysical data of imidazolinone-based fluorophores 1–60 illustrated on Fig. 9–19, as free molecules in solutions or constrained in confined environments

	Initial status					Constrained status							
NO.	Sol.	λ_{abs}	λ_{em} (λ_{ex})	ε	Φ_f	Const. env.	λ_{abs}	λ_{em} (λ_{ex})	ε	Φ_f	α_f	Applications	Ref.
1	n.d.	n.d.	n.d.	n.d.	n.d.	Thin film or powdered crystalline state	~370	~465	n.d.	n.d.	>10	n.d.	103
	n.d.	n.d.	n.d.	n.d.	n.d.	Suspension in H_2O/CH_3CN (2 vol%)	~370	~450	n.d.	n.d.	n.d.	n.d.	104
2	n.d.	n.d.	n.d.	n.d.	n.d.	Thin film or powdered crystalline state	~370	~460[a] ~560[a]	n.d.	n.d.	>10	n.d.	103
	n.d.	n.d.	n.d.	n.d.	n.d.	Suspension In H_2O/CH_3CN (2 vol%)	~380	448	n.d.	1	n.d.	n.d.	104
3	n.d.	n.d.	n.d.	n.d.	n.d.	Thin film	~370	~560	n.d.	n.d.	>10	n.d.	103
	n.d.	n.d.	n.d.	n.d.	n.d.	Powdered crystalline state	~370	450–550	n.d.	n.d.	>10	n.d.	103
	n.d.	n.d.	n.d.	n.d.	n.d.	**MOF1** $Zn_3(BTC)_2$ (0.05 wt% encapsulation)	n.d.	463 (365)	n.d.	n.d.	n.d.	n.d.	85
	EtOH/DMSO (1 vol%)	367	490	13	0.2	RNA (1 mg mL^{-1} in HEPES)	n.d.	520 (370)	n.d.	n.d.	5[a]	RNA sensor	8
4	MeOH	354	697	n.d.	<0.1	Nanoaggregate in H_2O/THF (3 vol%)	361	578	n.d.	14	>900	n.d.	92
5	MeOH	355	701	n.d.	<0.1	Nanoaggregate in H_2O/THF (3 vol%)	367	582	n.d.	9	>900	n.d.	92
6	H_2O	349	n.d.	n.d.	<0.01	Cell membrane	n.d.	n.d.	n.d.	n.d.	n.d.	Cell imaging	92
7	MeOH	256, 441	505	n.d.	0.17	Mircrosheet crystals	n.d.	500	n.d.	9.86	n.d.	Cell imaging	90
8	MeOH	272, 349	648	n.d.	0.04	Mircrosheet crystals	n.d.	550	n.d.	3.37	n.d.	Cell imaging	90
9	MeOH	263, 345	573	n.d.	0.5	Mircrosheet crystals	n.d.	543	n.d.	31.65	n.d.	Cell imaging	90
10	Acetone	420	489	n.d.	0.11	Microfiber crystals	n.d.	592	n.d.	4.85	n.d.	Hg^+ detection	105
11	Toluene	n.d.	434 (374)	n.d.	0.11	Plate-shaped crystals	n.d.	449 (400)	n.d.	5.24	n.d.	2D waveguide, security ink	107
	n.d.	n.d.	n.d.	n.d.	n.d.	Needle-shaped crystals	n.d.	566 (402)	n.d.	4.89	n.d.	1D waveguide	107
12	Toluene	n.d.	434 (408)	n.d.	0.12	Thin needle-like crystals	n.d.	492 (456)	n.d.	2.93	n.d.	2D waveguide, security ink, fluorescent ink	107
	n.d.	n.d.	n.d.	n.d.	n.d.	Thick plate-like crystals	n.d.	620 (406)	n.d.	7.06	n.d.	1D waveguide, fluorescent ink	107
13	n.d.	n.d.	n.d.	n.d.	n.d.	Cocrystal 13A	n.d.	460 (390)	n.d.	3.45	n.d.	n.d.	106
	n.d.	n.d.	n.d.	n.d.	n.d.	Cocrystal 13BI	n.d.	465 (390)	n.d.	4.5	n.d.	Optical waveguide	106
	n.d.	n.d.	n.d.	n.d.	n.d.	Cocrystal 13BII	n.d.	545 (390)	n.d.	4.3	n.d.	n.d.	106
	n.d.	n.d.	n.d.	n.d.	n.d.	Cocrystal 13C	n.d.	570 (390)	n.d.	2.7	n.d.	n.d.	106
	n.d.	n.d.	n.d.	n.d.	n.d.	Cocrystal 13D	n.d.	575 (390)	n.d.	2.3	n.d.	n.d.	106
	n.d.	n.d.	n.d.	n.d.	n.d.	Cocrystal 13EI	n.d.	580 (390)	n.d.	0.15	n.d.	n.d.	106
	n.d.	n.d.	n.d.	n.d.	n.d.	Cocrystal 13EII	n.d.	680 (390)	n.d.	n.d.	n.d.	n.d.	106
	n.d.	n.d.	n.d.	n.d.	n.d.	Cocrystal 13F	n.d.	631 (390)	n.d.	0.25	n.d.	n.d.	106
14	n.d.	n.d.	n.d.	n.d.	n.d.	**MOF1** $Zn_3(BTC)_2$ (0.09 wt% encapsulation)	n.d.	449 (365)	n.d.	n.d.	n.d.	n.d.	85
15	DMF	n.d.	518 (365)	n.d.	n.d.	**MOF1** $Zn_3(BTC)_2$ (0.14 wt% encapsulation)	n.d.	525 (365)	n.d.	n.d.	n.d.	n.d.	85
16	n.d.	n.d.	n.d.	n.d.	n.d.	**MOF1** $Zn_3(BTC)_2$ (0.19 wt% encapsulation)	n.d.	531 (365)	n.d.	n.d.	n.d.	n.d.	85
17	n.d.	n.d.	n.d.	n.d.	n.d.	**MOF1** $Zn_3(BTC)_2$ (0.21 wt% encapsulation)	n.d.	599 (365)	n.d.	n.d.	n.d.	n.d.	85
18	n.d.	n.d.	n.d.	n.d.	n.d.	**MOF2** $Zn_4O(BDC\text{-}CHO)_3$ (PSM, coordination)	n.d.	490 (360)	n.d.	n.d.	n.d.	n.d.	85 and 86
	THF	n.d.	426 (365)	n.d.	< 1	**MOF3** $Zn_4O(BDC\text{-}HBI')_3$ (coordination)	n.d.	516 (365)	n.d.	n.d.	n.d.	n.d.	86
	n.d.	n.d.	n.d.	n.d.	n.d.	**MOF4** $Zr_6O_4(OH)_4(BDC\text{-}BI)_6$ (coordination)	n.d.	490 (360)	n.d.	n.d.	n.d.	n.d.	85
19	ACN	360	430	n.d.	0.03	**NMOF-808** $[Zr_6O_5(OH)_3(C_9H_3O_6)_2(HCOO)_5(H_2O)_2]$ (coordination)	372	560	n.d.	5.6	n.d.	Cell imaging	83

Table 1 (*continued*)

	Initial status					Constrained status							
NO.	Sol.	λ_{abs}	λ_{em} (λ_{ex})	ε	Φ_f	Const. env.	λ_{abs}	λ_{em} (λ_{ex})	ε	Φ_f	α_f	Applications	Ref.
20	ACN	362	435	n.d.	0.01	**NMOF-808** $[Zr_6O_5(OH)_3(C_9H_3O_6)_2(HCOO)_5(H_2O)_2]$ (encapsulation)	373	560	n.d.	1.8	n.d.	n.d.	83
21	MeOH	360	470	n.d.	0.29	CMP (TEB) Suspension in MeOH	360	440 (360)	n.d.	0.24	~1	n.d.	109
22	MeOH	360, 400	460, 632	n.d.	0.56	CMP (TEB) Suspension in MeOH	383	515 (390)	n.d.	0.82	1.5	n.d.	109 and 110
	n.d.	n.d.	n.d.	n.d.	n.d.	CMP (TPA) Suspension in MeOH	n.d.	n.d.	n.d.	n.d.	n.d.	Photocatalysis for CO_2 reduction	110
23	MeOH	396[a]	466[a] (395)	n.d.	n.d.	COP (DOIDB)	n.d.	540 (365)	n.d.	83	n.d.	Detection of 4-NA (LOD = 66 ppb) and TNP (LOD = 0.62 ppm)	111
	n.d.	n.d.	n.d.	n.d.	n.d.	COP (DOITP)	n.d.	540 (365)	n.d.	44	n.d.	n.d.	111
24	MeOH	400[a]	468[a] (400)	n.d.	n.d.	COP (TOIDB)	n.d.	525 (370)	n.d.	28	n.d.	n.d.	111
	n.d.	n.d.	n.d.	n.d.	n.d.	COP (TOITP)	n.d.	525 (370)	n.d.	73	n.d.	Detection of 4-NA (LOD = 62 ppb) and TNP (LOD = 0.52 ppm)	111
25	THF	371	428	n.d.	n.d.	Micelles of PEG-*b*-PMMA (encapsulation)	371	436	n.d.	n.d.	42–76	Cell imaging	84
26	PEG-**26**-PCL in THF	371	427	n.d.	n.d.	Micelles	371	441	n.d.	n.d.	55	Cell imaging	115
	PEG-**26**-PMMA in THF	371	425	n.d.	n.d.	Micelles	371	448	n.d.	n.d.	24	Cell imaging	114
27	PEG-g**27**-PMMA in THF	426	482	n.d.	0.4	Micelles	438	503	n.d.	2.3	n.d.	Multicolour cell imaging	116
	PEG-*b*-PNIPAM-**27** in H2O	459	529	n.d.	0.14	Micelles	449	526	n.d.	2.17	20	*Bacillus thermophilus* detection	112
28	PEG-g**28**-PMMA in THF	366	429	n.d.	0.4	Micelles	362	430, 488	n.d.	0.7	2.3–3	n.d.	116
29	PEG-g**29**-PMMA in THF	372	429	n.d.	1.3	Micelles	372	430, 493	n.d.	2.1	n.d.	Multicolour cell imaging	116
30	PEG-g**30**-PMMA in THF	394	447, 562	n.d.	0.8	Micelles	386	550	n.d.	7.6	n.d.	Multicolour cell imaging	116
31	PEG-g**31**-PMMA in THF	394	434, 589	n.d.	0.4	Micelles	385	587	n.d.	2.1	n.d.	Multicolour cell imaging	116
32	PEG-g**32**-PNIPAM in H_2O	395	549	n.d.	n.d.	Micelles	395	523	n.d.	n.d.	1.5–2.4[a]	n.d.	113
	PEG-*b*-PNIPAM-**32** in H_2O	395	538	n.d.	n.d.	Micelles	395	475	n.d.	n.d.	n.d.	Cell imaging	113
33	HEPES buffer	n.d.	535 (425)	n.d.	2	Cucurbit[7]uril encapsulation (1 : 2 host–guest assembly)	n.d.	535 (425)	n.d.	13	~7	Fluorescence anti-counterfeiting	117
34	water	366	447	n.d.	n.d.	tobacco mosaic virus	366	447	n.d.	n.d.	20[a]	n.d.	118
35	Benzene	n.d.	~425 (370)	n.d.	0.15	Octa acid cavitand in borate buffer of D_2O	n.d.	~425 (370)	n.d.	1	10[a]	n.d.	119
36	0.2 M NaCl	340	n.d.	n.d.	0.05	Sodium cholate (75 mM)	355	~430	n.d.	n.d.	212	Bile salt sensing	120
37	water	453	526	22.7	0.7	95% glycerol in water (438.4 cP)	453	526	23.1	12	13	Latent fingerprints and DNA identification	121
38	water	538	623	8.5	0.2	95% glycerol in water (438.4 cP)	538	623	10.3	12	42	Latent fingerprints and DNA identification	121
39	n.d.	n.d.	n.d.	n.d.	n.d.	Glycerol	533	630 (530)	39.05	22.1	n.d.	Protein aggregation detection	10
	Glycerol at 25 °C (972 cP)	540	632	36.2	22	Glycerol (−80 °C, 3×10^{11} cP)	540	632	n.d.	33	1.5	n.d.	89
39a	SOD1(V31A)-Halo-**39a** in buffer	533	630 (530)	39.05	2.6	SOD1(V31A)-Halo-**39a** aggregates	543	600 (530)	36.24	22	n.d.	Protein aggregation detection	10 and 89
40	Glycerol at 25 °C (972 cP)	450	518	23.72	3	Glycerol (−80 °C, 3×10^{11} Cp)	450	518	n.d.	36	11	n.d.	89
	Ethylene glycol	450	518	n.d.	0.3	Ethylene glycol/glycerol (80 wt%)	450	518	n.d.	n.d.	4	n.d.	61

Table 1 (*continued*)

	Initial status					Constrained status							
NO.	Sol.	λ_{abs}	λ_{em} (λ_{ex})	ε	Φ_f	Const. env.	λ_{abs}	λ_{em} (λ_{ex})	ε	Φ_f	α_f	Applications	Ref.
40a	n.d.	n.d.	n.d.	n.d.	n.d.	n.d.	n.d.	n.d.	n.d.	n.d.	n.d.	Protein aggregation detection	61 and 89
41	Ethylene glycol	485	630	n.d.	1.2	Glycerol	485	630	30	8	n.d.	n.d.	61
41a	n.d.	n.d.	n.d.	n.d.	n.d.	n.d.	n.d.	n.d.	n.d.	n.d.	n.d.	Protein aggregation detection	61
42	SOD1(A4V)-Halo-**42** in buffer	n.d.	670 (580)	n.d.	n.d.	SOD1(A4V)-Halo-**42** aggregates	n.d.	670 (580)	n.d.	n.d.	~5.6	Protein aggregation detection	69
43	SOD1(A4V)-Halo-**43** in buffer	n.d.	510 (470)	n.d.	n.d.	SOD1(A4V)-Halo-**43** aggregates	n.d.	510 (470)	n.d.	n.d.	~5.6	Protein aggregation detection	69
44	DMSO	495	602	n.d.	n.d.	Aggregated protein	n.d.	582	n.d.	29	10.3	Cardiac proteome aggregation detection	122
45	DMSO	495	607	n.d.	n.d.	Aggregated protein	n.d.	574	n.d.	16	3.8	n.d.	122
46	water	416	557 (410)	n.d.	0.4	Labeled Rec bound to Ca^{2+}	n.d.	(440)	n.d.	n.d.	n.d.	n.d.	124
47	water	434	575 (430)	n.d.	0.69	Labeled Rec bound to Ca^{2+}	n.d.	(460)	n.d.	n.d.	n.d.	n.d.	124
48	water	~393	~570 (380)	n.d.	0.6	Labeled Rec bound to Ca^{2+}	n.d.	(410)	n.d.	n.d.	n.d.	n.d.	124
49	EtOH/DMSO (1 vol%)	438	527	12.8	0.65	Human serum albumin (HSA)	n.d.	515 (450)	n.d.	n.d.	~10[a]	HSA sensor	8
50	Buffer (pH < 8)	n.d.	480	n.d.	n.d.	Bound to p53 protein	n.d.	484, 530	n.d.	n.d.	2.3–2.6	n.d.	87
	n.d.	n.d.	n.d.	n.d.	n.d.	Bound to SSB protein	n.d.	489, 535	n.d.	n.d.	2–3.2	n.d.	87
	HEPES buffer (pH 7.4)	n.d.	487 (394)	23.34	0.05	RNA aptamer	n.d.	529 (398)	23.39	6	n.d.	n.d.	95
	HEPES buffer (pH 7.4)	n.d.	485 (378)	n.d.	0.07	RNA aptamer (Chili)	n.d.	537 (400)	18	8	~12[a]	n.d.	139
51	Buffer (pH > 5)	n.d.	501	n.d.	n.d.	Bound to p53 protein	n.d.	496	n.d.	n.d.	2.1	n.d.	87
	n.d.	n.d.	n.d.	n.d.	n.d.	Bound to SSB protein	n.d.	501	n.d.	n.d.	2	n.d.	87
	HEPES buffer (pH 5.5)	n.d.	498 (405)	11.86	0.07	RNA aptamer (Spinach)	n.d.	501 (469)	24.27	72	n.d.	Live cell imaging	95
	HEPES buffer (pH 7.4)	n.d.	489 (423)	30.1	0.07	RNA aptamer (Spinach2)	n.d.	501 (447)	22	72	n.d.	Live cell imaging	126 and 127
	n.d.	n.d.	n.d.	n.d.	n.d.	RNA aptamer (Baby Spinach)	n.d.	503 (466)	n.d.	n.d.	n.d.	n.d.	80
52	HEPES buffer (pH 7.4)	n.d.	495 (426)	35.4	0.1	RNA aptamer (Spinach2)	n.d.	505 (482)	31	94	n.d.	Live cell imaging	127
	n.d.	n.d.	n.d.	n.d.	n.d.	RNA aptamer (Broccoli)	469	507 (472)	29.6	94	n.d.	n.d.	129
	HEPES buffer (pH = 7.5)	n.d.	495 (426)	35.4	0.1	DNA aptamer (Lettuce)	n.d.	505 (455)	32.4	10.9	~11	RNA detection (SARS CoV-2 RNA)	82 and 100
	n.d.	n.d.	n.d.	n.d.	n.d.	RNA aptamer (Squash)	n.d.	503 (452)	24.2	71	1064	n.d.	93
53	HEPES buffer (pH 7.4)	n.d.	515 (460)	34.8	0.12	RNA aptamer (Spinach2)	n.d.	523 (500)	29	12	n.d.	Live cell imaging	127
54	HEPES buffer (pH 7.4)	n.d.	561 (473)	19.8	0.06	RNA aptamer (Corn)	n.d.	545 (505)	29	25	n.d.	Live cell imaging	96
	n.d.	n.d.	n.d.	n.d.	n.d.	RNA aptamer (Orange Broccoli)	n.d.	562 (513)	34	28	n.d.	n.d.	96
	n.d.	n.d.	n.d.	n.d.	n.d.	RNA aptamer (Red Broccoli)	n.d.	582 (518)	35	34	n.d.	n.d.	96
	n.d.	n.d.	n.d.	n.d.	n.d.	DNA aptamer (Lettuce)	n.d.	560 (510)	n.d.	n.d.	~11	n.d.	82 and 100
	n.d.	n.d.	n.d.	n.d.	n.d.	RNA aptamer (Squash)	n.d.	562 (495)	24.6	60	550	n.d.	93
55	HEPES buffer (pH 7.5)	n.d.	544 (455)	n.d.	0.33	RNA aptamer (Chili)	n.d.	545, 594 (463)	20	8	~14[a]	n.d.	139
56	HEPES buffer (pH 7.5)	n.d.	486 (379)	n.d.	0.11	RNA aptamer (Chili)	n.d.	542 (413)	21	40	~86[a]	Live cell imaging	139
57	HEPES buffer (pH 7.5)	n.d.	546 (436)	n.d.	0.1	RNA aptamer (Chili)	n.d.	592 (456)	22	10	~27[a]	Live cell imaging	139
58	HEPES buffer (pH 7.4)	n.d.	600 (460, 560)	n.d.	n.d.	RNA aptamer (Clivia)	n.d.	580 (524)	33	48	286	Live cell imaging	130 and 131
59	HEPES buffer (pH 7.4)	n.d.	582 (382), 594 (554)	n.d.	n.d.	RNA aptamer (Clivia)	n.d.	572 (497)	n.d.	n.d.	n.d.	Live cell imaging	130 and 131
	Tris buffer (pH 8)	n.d.	576 (501)	19.2	0.7	DNA G-quadruplex (NG 16)	n.d.	590 (503)	17.35	31	47	n.d.	99
60	Tris buffer (pH 8)	n.d.	600 (517)	38.8	0.5	DNA G-quadruplex (NG 16)	n.d.	612 (521)	37.5	30	63	n.d.	99
61	Tris buffer (pH 8)	n.d.	570 (500)	18.2	0.7	DNA G-quadruplex (NG 16)	n.d.	583 (499)	16.95	37	51	n.d.	99

Table 1 (*continued*)

	Initial status					Constrained status							
NO.	Sol.	λ_{abs}	λ_{em} (λ_{ex})	ε	Φ_f	Const. env.	λ_{abs}	λ_{em} (λ_{ex})	ε	Φ_f	α_f	Applications	Ref.
62	Tris buffer (pH 8)	n.d.	594 (511)	32	0.5	DNA G-quadruplex (NG 16)	n.d.	606 (513)	28.2	39	75	One- and two-photo bio-imaging in living cells and tissues	99
63	Tris buffer (pH 8)	n.d.	614 (540)	23.89	0.3	DNA G-quadruplex (NG 16)	n.d.	620 (538)	22.8	19	68	n.d.	99
64	Tris buffer (pH 8)	n.d.	662 (548)	16.12	0.1	DNA G-quadruplex (NG 16)	n.d.	668 (547)	15.5	3.2	29	n.d.	99
65	HEPES buffer (pH 7)	n.d.	~620 (545)	n.d.	n.d.	DNA aptamer (Lettuce)	n.d.	~620 (545)	n.d.	n.d.	n.d.	n.d.	82
66	MeOH	376	~450 (380)	n.d.	n.d.	DNA triplex	n.d.	465	n.d.	n.d.	5.8	DNA triplex detection	88
67	MeOH	377, 430	500 (430)	n.d.	n.d.	DNA triplex	n.d.	502	n.d.	n.d.	1.8	DNA triplex detection	88
68	HEPES buffer	347, 422	420 (337), 502 (447)	n.d.	n.d.	RNA aptamer	n.d.	420	n.d.	n.d.	5.7	RNA detection (LOD = 100 nM)	91
69	Tris buffer	n.d.	617 (470)	n.d.	n.d.	G-Quadruplex (NG 16)	n.d.	617 (470)	n.d.	n.d.	19	n.d.	98
70	Tris buffer	n.d.	462 (399), 595 (530)	n.d.	n.d.	G-Quadruplex (NG 16)	n.d.	462 (399), 595 (530)	n.d.	n.d.	48	n.d.	98
71	Tris buffer	n.d.	490 (399), 613 (560)	n.d.	n.d.	G-Quadruplex (NG 16)	n.d.	490 (399), 613 (560)	n.d.	n.d.	52	Ratiometric G-quadruplex imaging in living cells	98
72	HEPES (Ph 7.4)	n.d.	500 (425)	42.5	0.05	RNA aptamer (Broccoli)	n.d.	505 (470)	33.6	66.9	n.d.	Cell imaging	97
73	PBS buffer	~440	515 (434)	10.95	1	Glycerol	~440	515 (434)	18.02	13	13	Detection of mitochondrial viscosity	132
74	PBS-EtOH (30 vol%)	456	556	5.83	5.6	Glycerol	n.d.	n.d.	n.d.	12	2	Labelling endoplasmic reticulum	94
75	PBS/glycerin (0.2% DMSO, 7.9 cp)	n.d.	618 (550)	n.d.	n.d.	PBS/glycerin (0.2% DMSO, 438.4 cp)	n.d.	618 (550)	n.d.	n.d.	12	Dual-detection of viscosity and cysteine	133

[a] Data estimated by this review's authors. Abbreviates: Sol., solvents or solutions of dyes or compounds containing dyes for measurements; Const. env., constrained environments for measurements. Parameters: wavelengths of absorption, fluorescence emission, and fluorescence excitation (λ_{abs}, λ_{em}, λ_{ex}, nm); absorption coefficients (ε, 10^3 M^{-1} cm^{-1}); fluorescence quantum yield (Φ_f, %); fluorescence amplification factors (α_f).

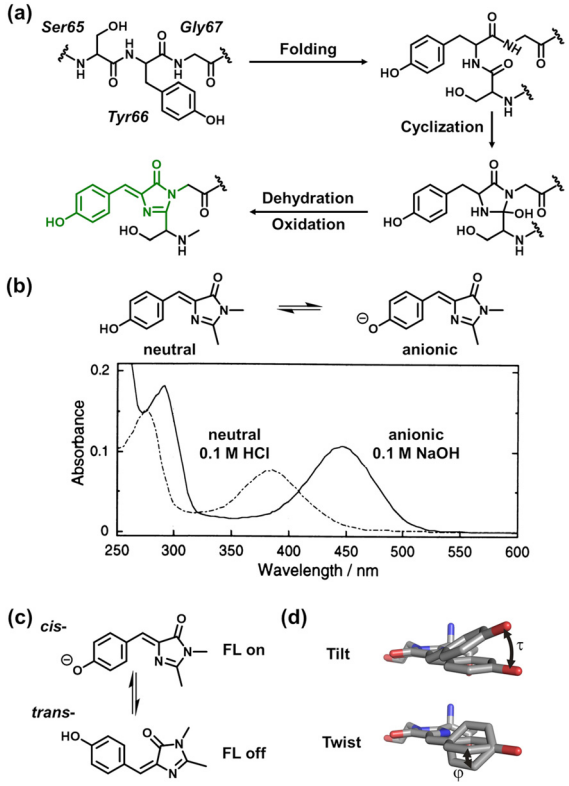

Fig. 2 Properties of 4-hydroxybenzylidene-2,3-dimethylimidazolinone (*p*-HBDI). (a) Mechanism of the chromophore biosynthesis. (b) Neutral or anionic forms of the chromophore *p*-HBDI during the ESPT process and absorption spectrum of GFP digest in 0.1 M NaOH or HCl.[18] Copyright 1996 National Academy of Sciences. (c) *Cis–trans* isomerization of the chromophore in GFP; (d) deviations from chromophore planarity: tilt and twist angles.[6] Copyright 2008 Elsevier Ltd.

isolated bioinspired imidazolinone-based fluorophores (Fig. 4), including the synthetic strategies and the key points to customize their fluorescence properties.

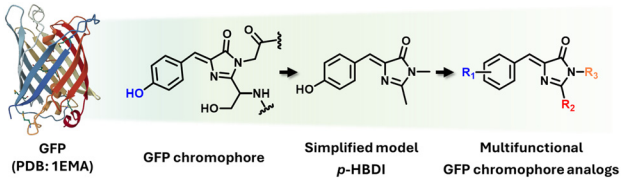

Fig. 4 The inspiration from GFP to multifunctional imidazolinone-based dyes.

3.1. Dye syntheses

As with any emissive dyes, substitutions or extensions of its conjugated structure exert considerable influence on the fluorescence properties of the GFP chromophore. A variety of imidazolinone-based fluorophores have thus been synthesized and characterized to match the color palette of fluorescent proteins.[8,33] More precisely, their photophysical properties are tailored by modifications on position of R_1, R_2, and R_3 (Fig. 4).[8,9,34,35] Numerous synthetic strategies were explored to obtain these fluorophores, mainly including Erlenmeyer azlactone method, Knoevenagel condensation, and [2+3] cycloaddition (Fig. 5).

The Erlenmeyer azlactone method is a well-established two-step approach for dye synthesis, also known as the Niwa synthesis (Fig. 5).[36] First, azlactones, also called oxazolones, are produced by the reaction of aromatic aldehydes and *N*-substituted glycine in the presence of anhydrous sodium acetate and acetic anhydride. Subsequently, the obtained oxazolones undergo a further reaction with a primary amine in the presence of potassium carbonate (K_2CO_3) under reflux in ethanol (EtOH), ultimately yielding dyes that are analogous to the GFP chromophore. The crucial one-pot reaction to synthesize imidazolinones could also be promoted by sodium acetate and acetic anhydride,[37] acetic acid,[38] zinc chloride,[39] pyridine,[40] and microwave.[41] In certain cases, the one-pot reaction from oxazolones to imidazolinones can be divided

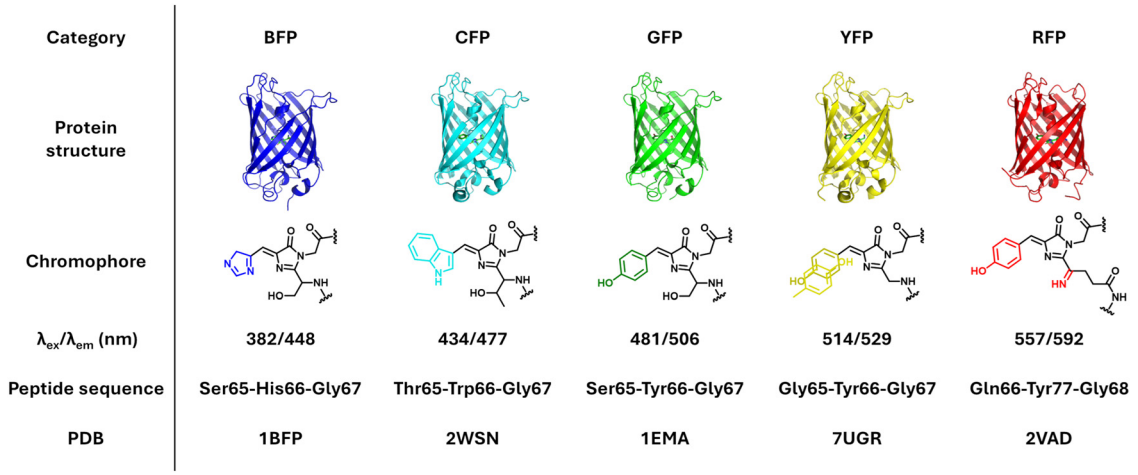

Fig. 3 Structural and photophysical features of representative fluorescent proteins. Shown are protein structures, chromophore compositions, excitation/emission maxima, peptide sequences, and PDB identifiers for BFP, CFP, GFP, YFP, and RFP. The structural information was acquired from Protein Data Bank (PDB).

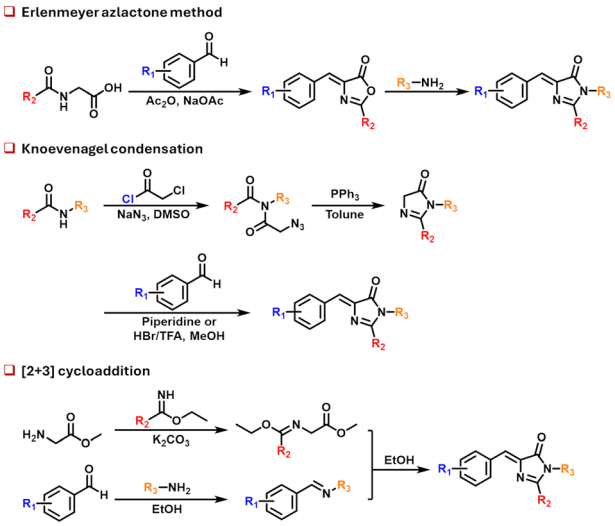

Fig. 5 Various methodologies for the synthesis of multifunctional imidazolinone-based fluorophores, enabling the manipulation of R_1, R_2, and R_3 using diverse reactants, including Erlenmeyer azlactone method, Knoevenagel condensation, and [2+3] cycloaddition.

into two sequential independent reactions: a ring-opening reaction and a cyclization reaction.[42] The amine-attacking ring-opening of oxazolones can occur readily in ethanol at room temperature, and the cyclization can then be conducted under the same conditions as the one-pot reaction. This two-step approach possibly enhances the purity and yield of final products.

The Knoevenagel condensation is an effective method for the synthesis of imidazolinones (Fig. 5). In this process, an imidazolinone devoid of C4 substitutions is initially obtained through the self-cyclization of an azide-containing amino acid, which is catalyzed by triphenylphosphine.[43,44] It subsequently reacts with aldehydes in the presence of piperidine or HBr/TFA/MeOH.[44] The addition of aldehydes to heterocycles can also be facilitated by ionic liquids[45] and $TiCl_4$.[46] This method has been demonstrated to be effective for a range of aldehydes, affording relatively high yields.[44,46] However, sodium azide, which is used during the first synthetic step in the preparation of 1,2-dimethyl-1*H*-imidazol-5(4*H*)-one, is extremely toxic and explosive and must therefore be handled and disposed of with great care.[44,47]

The [2+3] cycloaddition is another convenient method for imidazolinones syntheses between a Schiff-base and a methyl 2-(1-ethoxyethylideneamino)acetate (MEEA) (Fig. 5).[48] The Schiff-bases can be obtained by reactions of primary amines and aromatic aldehydes, and the MEEA can be afforded by reactions of methyl glycinate hydrochloride and ethyl acetimidate hydrochloride in the presence of K_2CO_3.[49] Numerous GFP chromophore analogs have been synthesized through this method.[8,50] Furthermore, Clark *et al.* introduced ethyl benzimidate hydrochloride instead of ethyl acetimidate hydrochloride to synthesize benzyl-modified precursors,[51] thereby affording dyes with elongated conjugated systems.[52] This is a facile and convenient method to tune the functional groups, which has become a prevalent method in the synthesis of GFP chromophore analogs.

3.2. Molecular strategies to tune the photophysical properties

The GFP fluorophore has mainly been synthesized either to understand the photophysics of this molecule or to synthesize materials with biological applications. In this context, particularly for medical imaging, absorption and excitation wavelengths that are as red-shifted as possible are preferred. To this end, the main strategies involve modifying the nature of the electron-donating groups (preferably at position R_1) and electron-withdrawing groups (preferably on the imidazolone, at position R_2), as well as extending the conjugated π-system. Additionally, since the dye is subject to TICT (twisted intramolecular charge transfer), it is possible to rigidify the chromophore structure by introducing bulky, coordinating or hydrogen bonding groups. This will have little or no effect on the chromophore's color but will modify its fluorescence efficiency (Φ_f, τ). Of note, R_3 position is not conjugated to the emissive core, so modifications on this position will have no effects on the isolated dye absorption and emission bands. However, it can be used to incorporate the dye in the matrixes and thus restrict movements, increase fluorescence efficiency (*vide infra*) and eventually prevent the formation of excimers.

Similar to the the GFP, a significant number of synthetic *p*-HBDI present a phenol on the *para* (R_1) position. Since the pK_a of this phenol (~8) is higher than physiological pH, *p*-HBDI-based dye would not be fluorescent without undergoing the ESPT process. This phenomenon is strongly influenced by hydrogen bond donor or acceptor motifs near the hydroxyl group.[20,53–58] Laptenok *et al.* reported that the di-fluoro (*meta*)–substituted *p*-HBDI (dye **51**, Table 1) exhibited a reduced pK_a of 5.4, leading to an ultrafast (50 fs) ESPT in the neutral form.[20] Then, Liu *et al.* systemically investigated the substituent effects on the fluorescence properties of *p*-HBDI-based fluorophores by introducing electron-withdrawing groups (fluorine) and electron-donating EDG (methoxy groups) on the phenyl ring.[58] The incorporation of fluorine on the *ortho* position increased the photoacidity (pK_a = 6.9) and the *o*-difluorination (pK_a = 5.7) resulted in an ultrafast barrierless ESPT process. By contrast, the methoxy groups led to ultrafast ESPT with weak photoacidity (pK_a = ~8). However, the Φ_f values of these *p*-HBDI derivatives are still very low (<0.1%) in aqueous solutions.

Apart from *p*-HBDI-based fluorophore, a variety of other substitutions have also been attempted at the position R_1 to improve the fluorescence efficiency (Φ_f > 10%, Fig. 6).[8,9,34,35] Compared to *p*-HBDI (Φ_f < 0.1%), fluorophores containing *meta*-dimethylamino or *para*-cyano was observed with remarkably enhanced Φ_f up to 46% (in hexane) and 25% (in ethanol with 1% DMSO), respectively. In addition, the phenolate of *p*-HBDI could be replaced by the naphthyl group to exhibit better fluorescence efficiency (Φ_f = 21% in ethanol with 1% DMSO). Moreover, for the dye decorated with the aromatic rings at the position R_2, the introduction of cyano, methoxycarboxyl and trifluoromethyl at the position R_1, respectively, could lead to higher Φ_f varying from 14% to 30% in dioxane.

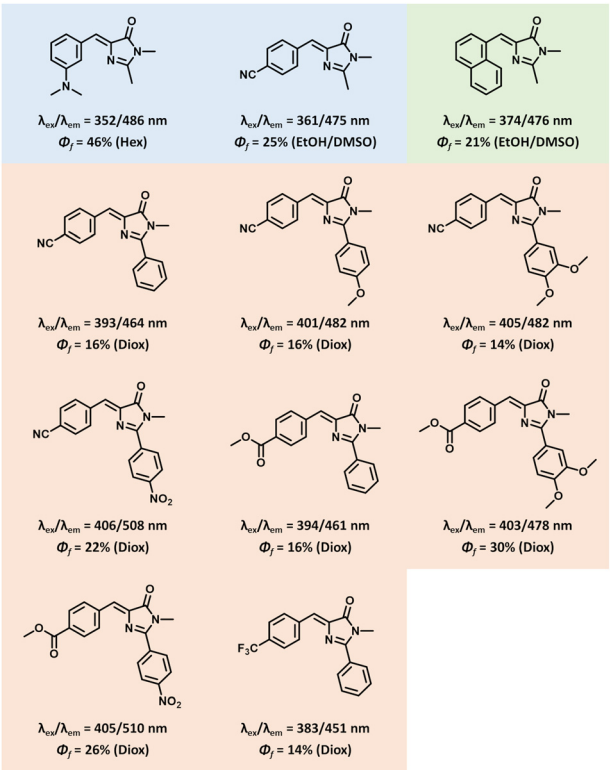

Fig. 6 Examples of imidazolinone-based fluorophores with Φ_f > 10%. Blue: R_1-subsitutions instead of the hydroxyl group of HBDI including *meta*-dimethylamino (*m*-ABDI) and *para*-cyano; green: containing naphthyl group instead of the phenolate of HBDI; red: R_1-subsitutions instead of the phenolate of HBDI and introduction of aromatic groups at the position R_2. Quantum yields are measured in hexane (Hex) or in ethanol with 1% DMSO (EtOH/DMSO), or in dioxane (Diox).

Beyond enhancing fluorescence efficiency, extending π-conjugation has been employed to redshift emission and broaden the scope of applications. Numerous fluorophores have been synthesized using a variety of building blocks, such as cinnamaldehyde derivatives at the R_1 position and *N*-substituted glycines at R_2, featuring aromatic or extended π-conjugated systems (Fig. 7a).[59–62] For example, Ye *et al.* introduced longer π-structures between the imidazolinone and aromatic rings using 4-dimethylaminocinnamaldehyde *via* Erlenmeyer azlactone method.[61] Compared to the dye with one methine group (dye **40**, Table 1, $\lambda_{ex}/\lambda_{em}$ = 450/518 nm), dye **41** emitted at 630 nm under λ_{ex} at 485 nm (Fig. 7a and Table 1). In addition, Tonge *et al.* acylated the glycine with crotonic acid (**M1**) and 2,4-hexadienonic acid (**M2**), thereby extending the conjugated structure of HDBI at position R_2 to mimic the emission of red fluorescence proteins (Fig. 7a).[62] Compared to *p*-HBDI, such modification resulted in longer wavelengths of the absorption and emission bands from dye **M1** to **M2** in both neutral and anionic forms. The neutral form of **M1** emit a blue fluorescence ($\lambda_{abs}/\lambda_{em}$ = 401/460 nm), while the anionic form presents a green emission ($\lambda_{abs}/\lambda_{em}$ = 460/530 nm). For **M2**, which features an elongated π-conjugated structure, these bands are red-shifted to 421/523 nm (neutral form) and 482/565 nm (anionic form).

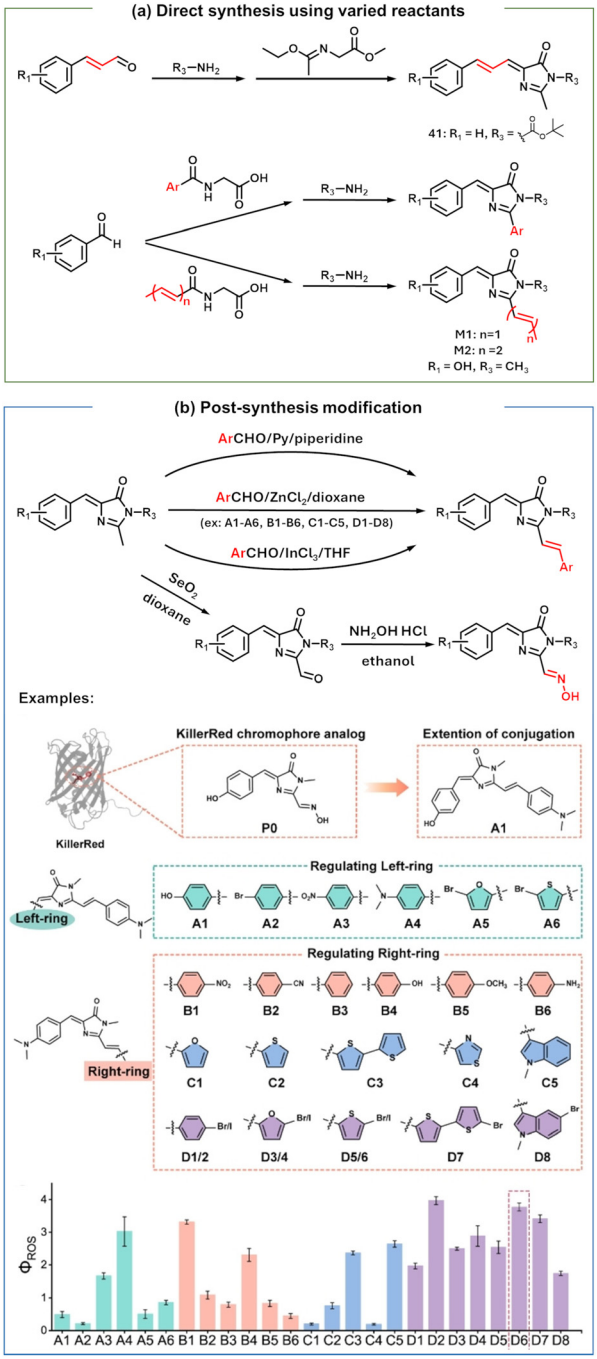

Fig. 7 Two strategies to elongate the π-structure of imidazolinone-based fluorophores including (a) the direct synthesis using varied reactants.[59–62] or (b) the post-synthesis modification.[63–66] Examples were achieved by (a) using the modified aldehyde (**41**)[61] or *N*-substituted glycine (**M1** and **M2**)[62] and (b) manipulating the left and right rings of π-extended dyes for tunable ROS generation efficiency (Φ_{ROS}).[65] Copyright 2022 Wiley-VCH GmbH.

Elongating the π-conjugated structure can also be achieved through the post-synthesis modification of the methyl group on the imidazolinone heterocycle. This modification can be catalyzed by pyridine (Py)/piperidine,[63] $ZnCl_2$,[64,65] and Indium(III) chloride ($InCl_3$)[66] or achieved by combining an oxidation of the methyl groups to aldehydes using SeO_2 and further reaction

with NH_2OH hydrogen chloride salts (Fig. 7b).[65] Facilitated by these methodologies, Feng and coworkers synthesized a series of imidazolinone-based fluorophores with extension of the conjugated structure at position R_2 to mimic functions of KillerRed (a protein featuring triplet excited state) for ROS generation (Fig. 7b).[65] They first explored the dimethylamino-decorated fluorophore (**A4**, Fig. 7) on the position R_1 led to better ROS generation efficiency (Φ_{ROS}), which could be further manipulated by the functionalization of the ring at position R_2. Notably, dye **D6** (Fig. 7) proved effective in both chromophore-assisted light inactivation and photodynamic therapy.

All the modifications briefly mentioned above aim at tuning the intrinsic spectroscopic properties of the fluorophore, such as its absorption and emission wavelengths, and ESPT. Although some modifications have succeeded in increasing the fluorescence quantum yield, the main drawback of the free dyes is the tendency to lose energy through non-radiative pathways (k_{nr}) due to TICT mechanism dyes (Fig. 8a).[23,67] As a result, these dyes are classified as rotor-based fluorophores, a feature that has been effectively leveraged in the design of viscosity-sensitive probes.[68,69] However, in certain applications, a fluorophore that remains emissive under all conditions is required. Before describing the fluorophore's incorporation into materials, we summarize here a few molecular strategies for restricting the tortional relaxations of dyes.

First, the steric effects of several groups at the position R_1 have been explored. Tsai *et al.* discovered that the introduction of cyano (CN) groups at the *ortho* positions of *meta*-dimethylamino-decorated dyes could effectively slow down the photoisomerization reaction (the τ torsion) with the increase in Φ_f from 46% to 60% in hexane and the decrease in the k_{nr} value from 0.24×10^8 s^{-1} to 0.16×10^8 s^{-1}.[34] In addition, Deng and coworkers also identified the self-restricted GFP chromophore analogs with 2,5-dialkoxyl substitutions (such as dye **32**, Table 1), exhibiting decent fluorescence efficiency ($\Phi_f = \sim 10\%$) in ethyl acetate compared to single or triple modifications of methoxy groups ($\Phi_f < 1\%$).[35] The longer alkoxyl groups could slightly increase the fluorescence efficiency in ethyl acetate, while the halogen or alkyl groups led to lower Φ_f ($< 4\%$).

The emissive behavior of imidazolinone-based fluorophores can be tuned by restricting intramolecular rotation. First, S. Chatterjee and P. Karuso synthesized a series of locked GFP chromophore analogs by using alkyl chains to replace protons on the exocyclic double bond and at the C2 position of the phenyl ring.[70] The introduction of ethyl or propyl groups resulted in higher Φ_f values in water and *tert*-butanol compared to analogs bearing protons or methyl groups, due to steric hindrance of single-bond rotation. However, the Φ_f values of all dyes remained very low ($< 0.3\%$). In a different structural context, ***o*-HBDI** provides an alternative strategy to enhance fluorescence. The presence of an *ortho*-hydroxyl group enables the formation of a seven-membered intramolecular hydrogen bond between the phenyl ring and the imidazolinone core, which restricts double-bond rotation (Fig. 8b).[71] This rigidification renders ***o*-HBDI** more emissive than the GFP chromophore (*p*-HBDI), with $\Phi_f \approx 0.3\%$ and $\tau = 38$ ps in toluene, and

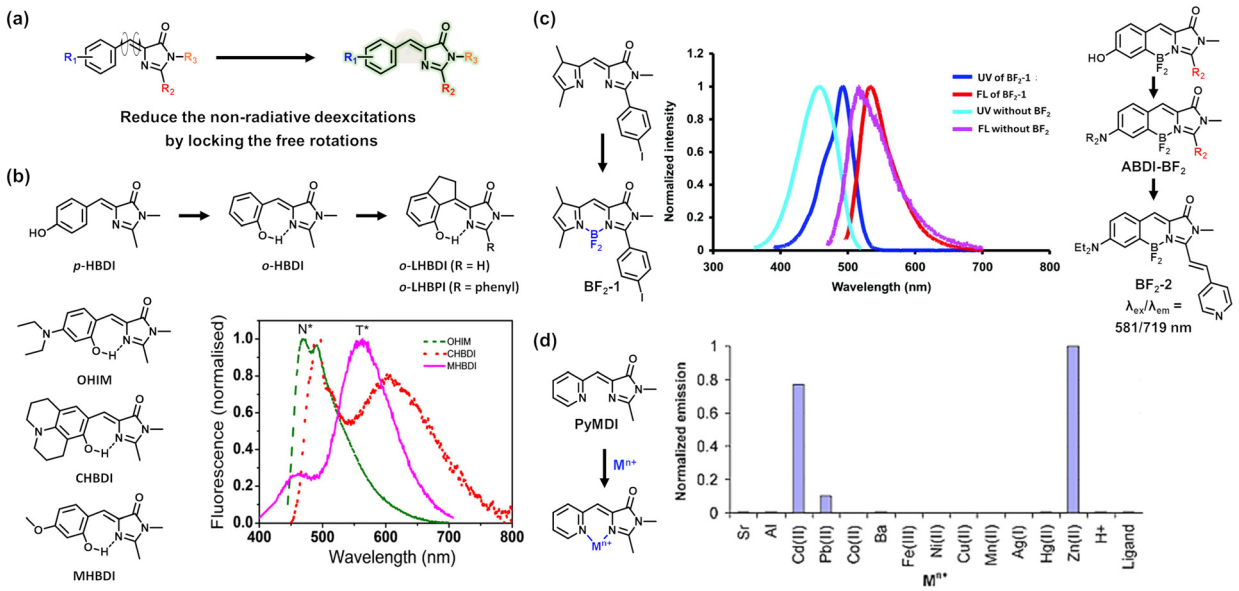

Fig. 8 Molecular strategies to improve the fluorescence efficiency of imidazolone-based dyes. (a) Suppression of non-radiative pathways by reducing or locking the dye rotation to improve the fluorescence efficiency of GFP chromophore analogs. (b) ***o*-HBDI**-based fluorophores. The inspiration from GFP chromophore (*p*-HBDI) to ***o*-HBDI** with a seven-membered ring hydrogen bond and the doubly locked fluorophore ***o*-LHBDI** and ***o*-LHBPI** further containing a covalent five-membered ring. Chemical structures of three ***o*-HBDI**-based fluorophores with other substitutions on the R_1 position and their fluorescence spectra presenting the bands of the charge transfer (N*) and the proton transfer (T*).[72] Copyright 2016 American Chemical Society. (c) BF_2-bridged fluorophores. Absorption and fluorescence emission of the rigidified dye **BF_2-1** compared to the unrestricted dye.[44] Copyright 2008 American Chemical Society. The innovation of **ABDI-BF_2**, especially for **BF_2-2** with the long emission wavelength in acetonitrile. (d) Fluorescence emission of **PyMDI** in mixed methanol/water (v : v = 1/1) at the concentration of in 15 mM in response to various cationic species.[45] Copyright 2010 The Royal Society of Chemistry.

additionally enables excited-state intramolecular proton transfer (ESIPT), leading to tautomer emission around 600 nm. The substitution of such *para*-substituted ***o*-HBDI** can further modulate the emission, while still limiting rotation around de C=C bound.[72] **CHBDI** (*para*-cyclicamino) displays dual fluorescence with a charge-transfer (CT) band below 520 nm and a proton-transfer (PT) band near 600 nm; **OHIM** (*para*-diethylamino) shows only CT emission between 467–505 nm; and **MHBDI** (*para*-methoxy) exhibits a stronger PT band near 567 nm. However, as in the previous examples, their fluorescence efficiencies remain very low (Φ_f = 0.65%, 0.33%, and 0.12% in toluene, respectively) with short lifetimes ($\sim$30 ps).

To overcome these limitations, a doubly restricted derivative, ***o*-LHBDI**, was designed by introducing a covalent five-membered ring in addition to the seven-membered hydrogen-bonded ring. This dual constraint dramatically enhanced tautomer emission, resulting in a quantum yield of 18% and a fluorescence lifetime of 2.27 ns in toluene (Fig. 8b).[46] However, applying the same five-membered ring strategy to *p*-HBDI was ineffective in aqueous solution at pH 10 (Φ_f = 0.051, τ = 5.8 ps). Owing to its high efficiency, amplified spontaneous emission, and narrow monochromatic output, ***o*-LHBDI** has since been employed in ESIPT-based OLEDs. A phenyl-substituted derivative at R_2 position of the imidazolinone cycle, ***o*-LHBPI** (Fig. 8b), was also prepared using the covalent five-membered ring rigidification strategy.[73] This structural locking restricts rotation around the exocyclic double bond, enabling fluorescence at room temperature. Its quantum yield in water is about 500 times higher than that of the non-rigidified counterpart. In contrast to the methyl-substituted version, the phenyl derivative shows dual emission (cyan and red), making it suitable for highly sensitive ratiometric sensing and cellular fluorescence imaging. Since then, other variations of ***o*-LHBDI** and ***o*-LHBPI** showed tunable fluorescence by introducing bromide, iodine, and methyl groups at the *para*-position of the hydroxyl, which further demonstrates the importance of the electronic substitutions on their emissive properties.[74,75] *Meta*-dialkylamino substituted dyes (*m*-ABDIs, Fig. 6) were also dually rigidified by combing the covalent five-membered ring with a cyclic phenyl-amino ring to both lock the exocyclic C–C bond and the C–N bond rotations.[76] Compared to the dye with only cyclic C–N bond ($\lambda_{abs}/\lambda_{em}$ = 351/683 nm, Φ_f = 6%), the double-locked dye exhibited a high Φ_f of 43% ($\lambda_{abs}/\lambda_{em}$ = 417/635 nm) in acetonitrile. Further cell experiments demonstrated such doubly rigidified dye first stained cytoplasm before accumulating on the cell membrane.

Additional rigidification strategies have been explored, including the irreversible covalent incorporation of a BF_2 group, similar to the approach used in BODIPY dyes. Burgess *et al.* chelated a BF_2 to nitrogen atoms on the imidazolinone heterocycle and the pyrrole ring of dye **BF_2-1** (Fig. 8c).[44] The rigidified structure induces a red shift in both the absorption and emission bands, and increases Φ_f to 86% in methanol. The strategy using BF_2 was also adopted by Baranov and coworkers to bridge the phenyl and imidazolinone rings.[63,77,78] Among them dye (ABDI-BF_2) comprising an aminobenzylidene imidazolinone (ABDI core) exhibited red-shifted absorption and emission spectra, high Φ_f, and pH-independent emission (Fig. 8c). For example, the diethylamino-decorated **ABDI-BF_2** (R = Et) exhibited prominent variations of Φ_f values in different solvents (Φ_f = 3% in water, Φ_f = 72% in dioxane) and also held the promising potential in fluorescent labeling of cellular lipid organelles due to its properties of solvatochromism, lipophilicity and low phototoxicity.[77] Most particularly, the structurally extended dye **BF_2-2** showed the reddest emission (at 719 nm) in acetonitrile.[63]

A reversible rigidification between two nitrogen heterocycles can also be achieved by the formation of coordinative bonds using cationic metals. For instance, Baldridge *et al.* replaced the hydroxyphenyl moiety of HBDI with a pyridyl (**PyMDI**) offering suitable coordination sites for Zn^{2+} or Cd^{2+} ions, which could emit brighter fluorescence (150 fold for **Zn-PyMDI**) than that of mixtures with other metal ions (Fig. 8d).[45] An off–on fluorescent probe was also developed by Li *et al.* as a Zn^{2+} chemosensor, operating in the micromolar range, in which metal coordination induces restricted rotation between the 1,10-phenanthroline and imidazolinone heterocycles.[60] The introduction of an amine group at the *ortho*-R_1 position ((*Z*)-*o*-PABDI) also allows complexation with metals such as Zn^{2+};[79] however, the resulting seven-membered ring is non-fluorescent, in contrast to the six-membered rings formed by metal-complexed PyMDI.

4. Imidazolinone-based dyes in constrained environments

Although various molecular strategies have been implemented to customize the fluorescence properties of imidazolinone-based fluorophores, the majority of chemically synthesized GFP chromophore analogs still exhibit relatively low brightness due to the intrinsic TICT mechanism.[10] Therefore, confined environments inspired by the folded protein cage have also been considered as an alternative strategy to customize the fluorescence properties. Relevant examples are summarized in Table 1 and includes confinement by non-covalent interactions through H-bonds,[80–82] van der Waals interactions,[83–85] metal coordination,[85,86] or covalent, mainly in DNA,[87,88] protein scaffolds,[10,61,69,89] but also in synthetic porous matrices[83,85,86] or polymers.[10,89] Of note, the majority of studies focus on free dyes that are non-covalently encapsulated within their ''cage'' while only a small percentage (*ca.* 30%) involve dyes that are covalently bound. Table 1 compares the key spectroscopic properties (λ_{abs}, ε, λ_{ex}, λ_{em}, Φ_f) of discussed dyes in both free and confined states and includes the nature of confined environments and diverse applications. Most of the articles we reviewed focus on biological applications, especially for imaging or sensing, likely due to the bioinspired nature of the dyes.

In a nutshell, around 90% of the studies leverage the dyes' molecular rotor properties and their fluorescence enhancement to develop sensors (mainly used in cell imaging) and the remaining focus on phototherapy, photocatalysis, and optical devices. The absorption wavelengths range from *ca.* 250 nm[90]

to *ca.* 540 nm,[10] emissions wavelengths from *ca.* 420 nm[91] to *ca.* 700 nm.[92] While fluorescence quantum yields are only reported in *ca.* 70% of the cases, they are often below for the free dyes 1% and varies between few percent, up to more than 70% for dyes in constrained environments. Thus, fluorescence amplification factors (α_f) vary from 1.5 up to more than 1000.[93] Similarly, in most examples, the molar extinction coefficient (ε, M^{-1} cm^{-1}) is not reported, whose studied values range from 5000 M^{-1} cm^{-1} (ref. 94) to over 30 000 M^{-1} cm^{-1}.[10,89] In some cases, ε increases upon confinement, while the opposite tendency is observed in others. Such variation with the environment is common for push–pull type dyes or dyes subjected to excimer formation. Finally, one of the main disadvantages of GFP is its rapid photobleaching. Few studies have investigated the photobleaching behavior of such synthetic dyes, but when they do, acute photoresistance compared to fluorescent proteins or other organic dyes where reported.[93,95–100]

The following sections will detail some chosen examples, sorted by the nature of the confinement, starting from the simplest to the most complex, and highlighting potential applications.

4.1. Aggregates

The simplest way to form a material from a chromophore is to study it in powder or crystalline form. In such aggregated states, fluorophores are rigidified by their neighboring molecules, which reduces non-radiative deactivation pathways—a process particularly prevalent in isolated flexible fluorophores such as *p*-HBDI. This phenomenon, although now widely termed aggregation-induced emission (AIE), in fact represents a classical effect that has long been recognized.[101] However, aggregation can also lead to a decrease in fluorescence (aggregation-caused quenching, ACQ), most often due to π–π stacking. Therefore, a balance must be achieved, as the spatial organization of chromophores plays a crucial role in determining the photophysical properties of the resulting material.[102]

Hydrophobic derivatives of the GFP chromophore (**1–3**, Fig. 9) were explored by Tolbert *et al.* for their emission in the solid/crystalline state.[103] Alkyl-decorated fluorophores are nonfluorescent in solution with similar absorption maxima (~370 nm), but their solid-state luminescence strongly depend on the length of the *O*-alkyl chains. While non-alkylated HBDI remains nonfluorescent, dyes with longer chains (hexyl and dodecyl) show distinct emission features, and a progressive hypsochromic shift in crystal emission—from methoxy to hexyl to dodecyl—attributed to weakening electronic coupling between aggregated molecules. These synthetic analogs (**1** and **2**) were also used to prepare aqueous suspensions of needle-shape microparticles *via* a nanoprecipitation method, which became fluorescent due to the restriction of the free dye rotations.[104] The tendency to form nanofibers of dye **2** could be reinforced by the addition of poly(acrylic acid) thought no explanation about this phenomenon could be found. Both dispersions had $\Phi_f < 7\%$ in water. Similarly, Tou *et al.* developed fluorescent nanoparticles (d = 200–370 nm) from *m*-dialkylamino-decorated dyes **4** and **5** (Fig. 9).[92] These chromophores are known for

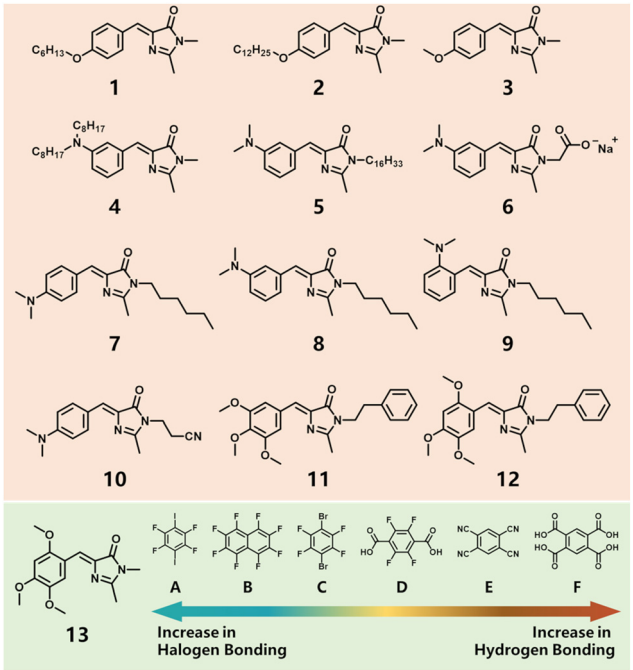

Fig. 9 Chemical structure of selected dyes confined in aggregates (**1–5** and **7–13**), a water-soluble derivative (**6**), and compounds (A)–(F)[106] used to form cocrystals with dye **13** by implementing diverse interactions of halogen or hydrogen bonding. See Table 1 for detailed spectroscopic data.

their positive solvatochromism, emits at ~620 nm in acetonitrile, while the nanoparticles emit at ~580 nm in water attributable to solvent–solute H-bonding. The nanoparticles exhibit quantum yields of approximately 10% and fluorescence lifetimes around 7 ns, making them promising candidates for bioimaging applications. The water-soluble dye **6** (Fig. 9) was further synthesized and could be used to stain cell membranes in fluorescence imaging.[92] Gan and coworkers prepared micro-needles of dyes **7–9** with different substituted positions on the phenyl ring by a solvent exchange method (MeOH/water).[90] Ultrahigh resolution cold field scanning electron microscopy revealed that the *p*-DBHI (**7**) and *o*-DBHI (**9**) formed micro-sheets, while the *m*-DBHI (**8**) assembled into hollow microtubes. All the dyes displayed almost no fluorescence in methanol ($\Phi_f < 0.2\%$), whereas their aggregated or solid-state forms showed strong luminescence, with quantum yields of 9.9%, 3.4%, and 31.7% for *p*-DBHI, *m*-DBHI, and *o*-DBHI, respectively. For cell imaging experiments, the dyes were solubilized in DMSO, and *p*-DBHI appeared to penetrate cells more effectively than the others.

Recently, Xu *et al.* developed a *m*-dialkylamino-decorated dye **10** bearing a CN group at the R_3 position, which forms microfibers *via* nanoprecipitation in water.[105] The dye exhibits low fluorescence in various organic solvents ($\Phi_f < 0.4\%$), whereas its assemblies in the solid state show a higher quantum yield of 4.9%. Notably, the presence of certain ions, such as Hg^{2+}, disrupts the formation of these microfibers, leading to fluorescence quenching. This property allows the dye to be adapted as a selective probe for Hg^{2+} detection.

Fluorescent crystals of trimethoxy-substituted dyes have also been investigated for optical material applications.[106–108]

Dabke *et al.* studied dyes **11** and **12**, which undergo thermal phase transitions and exhibit distinct photoluminescence in the crystalline state.[107] In solution, both dyes show very weak fluorescence with highest Φ_f values of 0.11% and 0.02% in toluene for dyes **11** and **12**, respectively. In contrast, their crystalline forms display strong emission. For dye **11**, plate-shaped crystals fluoresce at 449 nm (blue, λ_{ex} = 400 nm), whereas needle-shaped crystals show a red-shifted emission at 566 nm (yellow, λ_{ex} = 402 nm) due to stronger π–π interactions, with absolute quantum yields around 5% for both forms. Dye **12** forms thick plate-like crystals with red emission at 620 nm (λ_{ex} = 406 nm) and thin needles with emission at 492 nm (λ_{ex} = 456 nm); the thick plates have a higher quantum yield (Φ_f = 7%) compared to thin needles (Φ_f = 3%) because of enhanced π-stacking. Temperature-dependent studies revealed remarkable shifts in emission: dye 11's plate-shaped crystals red-shifted from blue (449 nm) to yellow (516 nm) upon heating, while dye 12's thick plate-like crystals showed a hyperchromic shift from green (492 nm) to orange (568 nm). These behaviors highlight their potential in optical waveguides and thermoresponsive fluorescent inks.

Finally, R. G. Gonnade *et al.* modulated the photoluminescence of dye **13** by tuning its staking states in the cocrystals with other aromatic molecules.[106] The dye **13** could form two crystalline states with compounds B and E, termed as 13BI/13BII and 13EI/13EII. The UV absorption maxima of these cocrystals located in the range between ~370 and 470 nm. Their emission wavelengths from cocrystal 13A to cocrystal 13EII was red-shifted from 460 nm (cyan) to 680 nm (dark orange), respectively (Table 1). Among them, Cocrystal 13BI exhibited the best quantum yield (of 4.5%) and was explored for the optical waveguide with the optical loss of 0.1063 dB μm^{-1}. Dye **13** was further used to fabricate visible-range photodetector, holding the great potential of single crystal GFP chromophore analogs for the applications in optoelectronics.[108]

4.2. Synthetic matrices

In the field of synthetic materials, porous frameworks are among the best candidates for mimicking the local environment of GFP, providing a structurally confined space that can stabilize the fluorophore and modulate its photophysical properties. In most examples, the porous cavities are host for the dyes, but in others, the dye is directly a building block of the material.

Metal–organic frameworks (MOFs) represent a family of synthetic porous *m*-aterials that can host dyes and enhance their fluorescence.[11] Shustova *et al.* developed several MOFs dopped with GFP chromophore analogs and focused on photophysical properties of those novel materials. They established a non-coordinative MOF-fluorophore complex using $Zn_3(BTC)_2$ (**MOF1**, BTC: benzene-1,3,5-tricarboxylate).[85] The three-dimensional pore sizes of **MOF1** were 10.8 and 11.5 Å (Fig. 11a), which was suitable for the immobilization of dyes **3** and **14–17** (Fig. 10). The immobilized dyes within frameworks demonstrated the capacity to recover fluorescence in the solid state, exhibiting a color palette varying from blue to yellow.

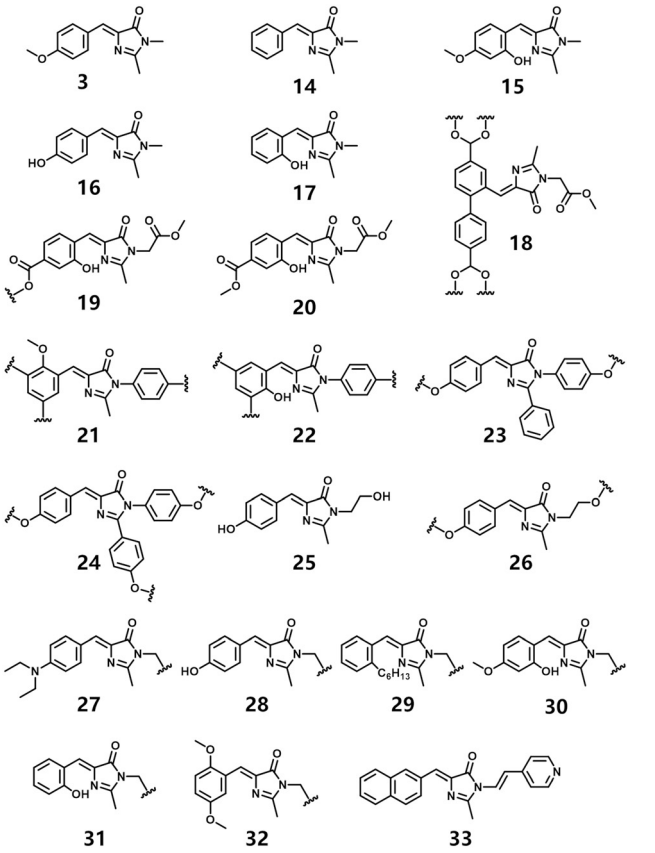

Fig. 10 Chemical structure of selected dyes confined in synthetic matrices, including MOFs (**3** and **14–20**), COPs (**21** and **24**), polymeric assemblies (**25–32**), and CB[*n*]s (**33**). The zigged lines indicate dyes are covalently linked to constrained systems. See Table 1 for detailed spectroscopic data.

Interestingly, the emission wavelength of **15** in the MOF scaffold was around 520 nm similar to that of the free dye in DMF. Compared to the solids of the dye itself (λ_{em} = 649 nm), the hypsochromic shift was attributed to the isolation of the dye **15** in the pores, thereby reducing π–π interactions between the phenyl and heterocycle groups.

Additionally, fluorophores have been engineered for incorporation into the MOF framework either through post-synthesis modification or direct coordinative synthesis (Fig. 11b). For example, Shustova's group utilized the pendent aldehyde groups of $Zn_4O(BDC\text{-}CHO)_3$ (**MOF2**, BDC-CHO: 2-formyl-biphenyl-4,4′-decarboxylate, Fig. 11) for the on-site synthesis of dye **18** (Fig. 10).[85,86] Approximately 5% of the aldehyde groups have been functionalized with dyes. They also inserted two carboxylic acid groups on dye **18** to coordinate Zn^{2+} or Zr^{2+} for the formation of the skeleton of $Zn_4O(BDC\text{-}HBI')_3$ (**MOF3**)[86] or $Zr_6O_4(OH)_4(BDC\text{-}BI)_6$ (**MOF4**), respectively (Fig. 11a).[85] Compared to the dye itself (λ_{em} = 426 nm), these fluorescent MOFs possessed an redshifted emission maximum similar to the natural GFP (λ_{em} = ~500 nm).

Finally, A. Singh *et al.* exploited the formate exchange to modify the synthetic MOF (**NMOF-808**, Fig. 11a) by reacting with the carboxylic acid group of dye **19** (Fig. 10).[83] Fluorophores were grafted on the MOF scaffold and immobilized

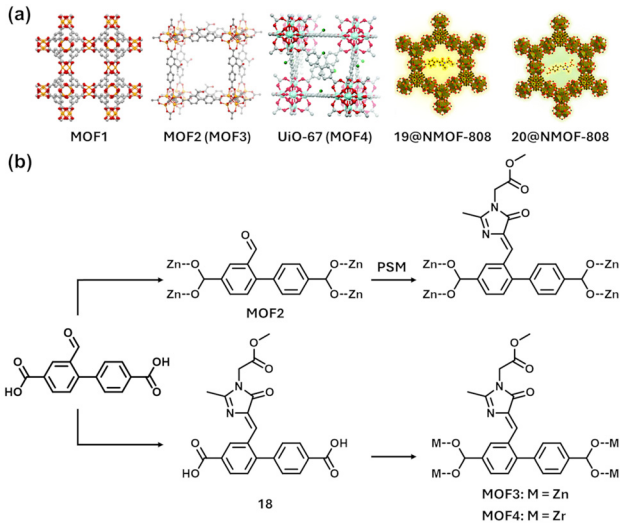

Fig. 11 MOF-based GFP analogs. (a) Fragments of the X-ray crystal structures of MOFs used to construct GFP analogs. MOF3 is isoreticular with MOF2, and MOF4 is isoreticular with UiO-67. Dye **19** is covalently grafted onto NMOF-808, whereas dye **20** is non-covalently encapsulated within NMOF-808.[83,85,86] Copyrights 2016 The Royal Society of Chemistry, 2015 and 2020 American Chemical Society. (b) Synthetic routes for coordinative immobilization of dye **18** within the skeleton of MOFs through post-synthesis modification (PSM) of **MOF2** and the direct coordinative synthesis of **MOF3** and **MOF4**.[86] See Table 1 for detailed spectroscopic data.

within the MOF pores, resulting in the emission of yellow light with a 100-fold increase in quantum yield and a remarkably longer excited lifetime from 0.03 ns to 1.5 ns. The covalent strategy for **19@NMOF-808** led to higher quantum yield and longer lifetime in comparison with **20@NMOF-808** (Fig. 9a) where dye **20** is encapsulated within the pores of **NMOF-808.**

The synthesis of fluorophores with specific substitutions can also be employed in the design of metal-free covalent organic polymers (COPs).[109–111] For this purpose, Maji and coworkers designed two imidazolinone-based fluorophores containing three iodine atoms (**21** and **22**, Fig. 10) for incorporation through Pd-catalyzed Sonogashira–Hagihara coupling in star-like conjugated microporous polymers (CMPs).[109,110] The advantage of such conjugation is that it extends the π-conjugated structure combined with a strong rigidity as evidenced by long luminescent lifetimes of the materials (∼4 ns) in comparison to that of free dyes (<1 ns). When dye **22** is combined with strong electron-donating group as triphenylamine,[110] the donor–acceptor system showed good light-harvesting capabilities, charge separation, and charge migration. Moreover, these conjugated microporous polymers display appropriate bandgaps and photoluminescence lifetimes, making them suitable for photocatalytic CO_2 reduction.[110] Recently, G. Anjum *et al.* developed four covalent organic polymers based on two di- (dye **23**) and trihydroxy- (dye **24**) substituted GFP chromophores.[111] The achieved polymers exhibit high solid-state quantum yields (up to 83%), similar to GFP (79%). The fluorescent materials can detect the nitroaromatic organic pollutants and explosives by fluorescence quenching

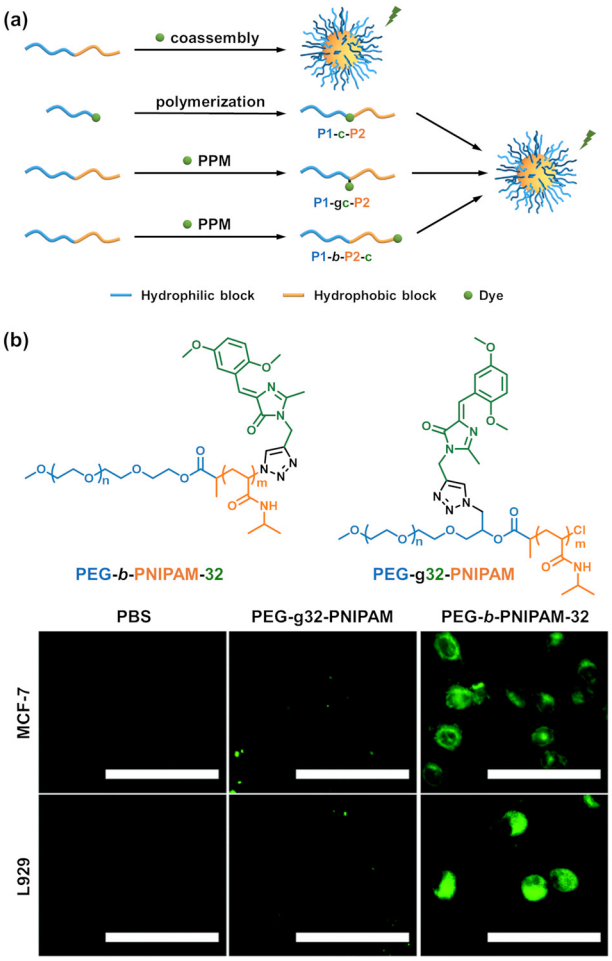

Fig. 12 Examples of imidazolinone-based dyes incorporated in synthetic linear polymers. (a) Strategies to construct GFP-like polymeric systems, including the coassembly of dyes and copolymers, the polymerization triggered by dye-labeled macroinitiators (**P1-c-P2**), and the post-polymerization modification (PMM) at the middle (**P1-gc-P2**) or terminal of copolymers (**P1-b-P2-c**), in which "c" stands for the dye, "gc" refers to the dye pendant on the polymer chain, and "PX" represents the block of copolymers. (b) Depict the modification of PEG-*b*-PNIPAM using 2,5-dimethoxy-decorated fluorophore **32** at the end of the polymer chain (**PEG-b-PNIPAM-32**) or the middle of two blocks (**PEG-g32-PNIPAM**) and the fluorescence imaging of MCF-7 and L929 cells with PBS buffer or incubation with 1 mg mL^{-1} polymers. λ_{ex} = 405 nm. Scale bar: 100 μm.[113] Copyright 2019 The Royal Society of Chemistry. See Table 1 for detailed spectroscopic data.

(∼80%) with a LOD for 4-nitroaniline (4-NA) and 2,4,6-trinitrophenol (TNP) at 0.062 and 0.52 ppm, respectively.

Fluorophores have also been incorporated into linear polymers, either at the chain end,[112,113] along the polymer backbone,[113–116] or were simply encapsulated[84] (Fig. 12). Most of these approaches were developed by Zhu's group. First, the *p*-HDBI derivate **25** (Fig. 10) was encapsulated in polymeric micelles of poly(ethylene glycol)-*b*-poly(methyl methacrylate) (PEG-*b*-PMMA) through the coassembly strategy.[84] Its fluorescence was activated during the self-assembly process. The increase in the fluorescence intensity is observed by reducing the ratio of tetrahydrofuran to water due to the gradual

formation of micellar structures. The fluorescence enhancement can also be promoted by increasing the length of the hydrophobic PMMA chain (α_f up to 76). These fluorescent micelles were further applicable for cell imaging. Zhu's group also introduced *p*-HBDI at the middle[113–116] or terminal[112,113] positions of amphiphilic diblock copolymers. These block copolymers are able to self-assemble into micelles, wherein the fluorescence of dyes is activated by the confinement of dyes within hydrophobic domains. Dye **26**, based on *p*-HBDI, was first modified with a hydroxyl group at R_3, then linked to PEG *via* phenolate chemistry (Fig. 10). This dye-labeled PEG acted as a macroinitiator for ring-opening polymerization of ε-caprolactone, yielding a PEG-*b*-PCL diblock copolymer with the dye positioned at the junction between the two blocks.[115] The functionalized amphiphilic block copolymer PEG-**26**-PCL exhibited weak fluorescence (λ_{em} = 427 nm) in THF. Upon micelle formation (d = 160 nm), its emission fluorescence was enhanced and red-shifted to 441 nm (λ_{ex} = 371 nm), attributed to the dye's close proximity. Additionally, the hydroxyl group of PEG capped with dye **26** was converted into a bromine function, enabling it to serve as a macroinitiator for the atom transfer radical polymerization (ATRP) of methyl methacrylate to produce amphiphilic PEG-*b*-PMMA. The functionalized PEG-**26**-PMMA displayed similar properties to PEG-**26**-PCL, with enhanced fluorescence (λ_{em} = 448 nm) upon micelle formation (d = 50 nm). They also functionalized block copolymers through azide–alkyne click chemistry.[112,113,116] Specifically, a series of amphiphilic diblock polymers, PEG-*b*-PMMA, were designed with a pendant azide group at the junction between the two blocks, enabling click-coupling with various dyes (**27**–**31**, Fig. 10) bearing a propargyl group at the R_3 position.[116] The resulting dye-labeled copolymers, PEG-gc-PMMA, were capable of forming multicolor fluorescent micelles (d = 25–65 nm) with emission wavelengths ranging from 430 to 587 nm, producing colors from blue to orange. These fluorescent micelles were both utilized for cell imaging.

Finally, HBDI fluorophores have also been incorporated into water soluble diblock copolymers containing thermoresponsive segments poly(*N*-isopropylacrylamide) (PNIPAM).[112,113] Upon heating, the dehydration of PNIPAM (T > 45 °C) promoted the micellization of copolymers with PEG as the corona and dehydrated PNIPAM as core, thereby enhancing the fluorescence of the dye in the rigidified structure.[112] Also, the higher the molar mass of PNIPAM is, the more fluorescent the assemblies become. Due to this property, PEG-*b*-PNIPAM-**27** were applied to indicate the high temperature environment of *Bacillus thermophilus* by the fluorescence increase, specifically at 70 °C. By using dye **32** (Fig. 10), the fluorescence emission of such thermosensitive objects could be tuned from ~450 to ~550 nm.[113] Also, the site-dependent fluorescence was observed that PEG-*b*-PNIPAM-**32** with the dye at the end of the polymer chain has more intense emission intensity than PEG-g**32**-PNIPAM with the dye at the junction between two blocks in living cells, probably due to less negative effects of the polymer backbone and a better movement restriction (Fig. 12b).

Finally, the macrocycles of cucurbit[*n*]urils (CB[*n*]s, n = 6, 7, and 8) have been utilized by Ren and Huang to offer a protein cage-like environment for the encapsulation of dye **33** (Fig. 10) *via* host–guest complexation.[117] The dye **33** contained a naphthalene ring to extend the conjugated structure and ensure the highly selective host–guest interactions within CB[*n*]s. The dye itself exhibited weak fluorescence in HEPES buffer ($\lambda_{ex}/\lambda_{em}$ = 425/535 nm, Φ_f = 2%). Upon adding CB[*n*]s, the emission intensity of dye **33** was significantly enhanced, especially using CB[7] to form 1 : 2 host–guest assembly with a highest α_f at ~7. The fluorescence enhancement can be reversed by adding amantadine hydrochloride to competitively bind with CB[7]. The reversible on–off fluorescence of CB[7]-**33** assemblies was further applied for the anti-counterfeiting on A4 paper.

4.3. Natural hydrophobic/lipidic cavities

Beyond synthetic matrices, HBDI chromophores have been grafted or encapsulated in natural amphiphilic structures or micelles. A notable example of covalent grafting involves the insertion of dye **34** (Fig. 13) in the hydrophobic central cavity (~4 nm) of the tobacco mosaic virus (TMV).[118] After conjugation, the emission intensity at 447 nm was remarkably enhanced (α_f = ~20), which was diminished by the disassembly of TMV in harsh environments (pH = 2.3 or 9.6).

Dye **35** has been confined within deep-cavity host molecules, such as octaacid (OA), a hydrophobic cavitand that forms a capsule-like dimer (~14 Å × 7 Å), mimicking the protective β-barrel structure found in GFP (Fig. 14a).[119] This encapsulation strategy leads to the significant fluorescence enhancement of dye **35** (α_f ~ 7), attributed to confinement-induced rigidification and restriction of the single-bond rotation (Φ angle, Fig. 2), and weak host–guest interactions, which collectively suppress internal conversion while preserving some flexibility for isomerization. In another approach, dye **36** bearing a trifluoromethyl substituent was embedded within the hydrophobic core of sodium cholate micelles (bile salts), exhibiting a dissociation constant of 74 mM (Fig. 14b).[120] This configuration yielded a remarkable α_f at 212, mainly due to inhibition of internal conversion, while still permitting some degree of isomerization, similar to the behavior seen in OA cavities.

Fluorescence enhancement of GFP chromophore analogs in lipidic or amphiphilic environments has also found application in biometric. Recently, Ruan *et al.* developed two positively

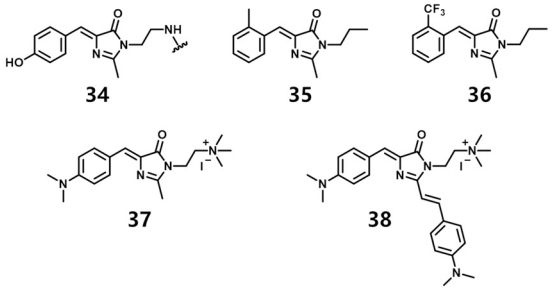

Fig. 13 Chemical structure of selected dyes confined in natural hydrophobic or lipidic cavities. The zigged lines indicate where the dyes are covalently linked to the constrained systems. See Table 1 for detailed spectroscopic data.

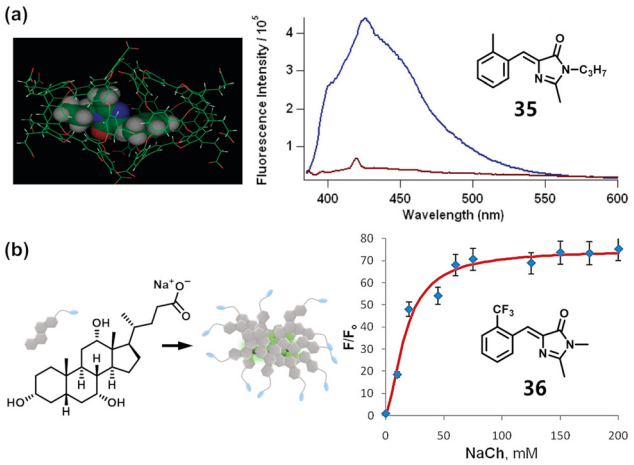

Fig. 14 Imidazolinone-based dyes constrained in hydrophobic/lipidic cavities. (a) Illustration of dyes encapsulated in OA and the fluorescence activation of dye **35** before and after the encapsulation.[119] (b) The illustration of NaCh aggregation to constrain dye **36** and its fluorescence enhancement by increasing NaCh concentration in 0.2 M NaCl aqueous solution.[120] Copyright 2010 and 2011 American Chemical Society. See Table 1 for detailed spectroscopic data.

charged *m*-dimethylamino-decorated dyes—a yellow-emitting (**37**) and a red-emitting (**38**)—for the rapid detection of latent fingerprints using a portable imaging device (Fig. 13).[121] By introducing ammonium groups at the R_3 position, the dyes exhibit strong binding affinity to negatively charged fatty acid components in fingerprints. With the red-emitting dye **38**, a 42-fold fluorescence enhancement was observed in glycerol, enabling visualization of fingerprints within 10 seconds using only 40 μM of the dye. Notably, these dyes do not contain pyridinium groups and metal ions, minimizing the risk of DNA contamination, which allowed for subsequent DNA extraction and genetic analysis.

4.4. Proteins

GFP chromophore analogs have naturally been investigated within protein environments, either through covalent attachment—most commonly *via* the HaloTag method[10,61,69,89]—or by targeting hydrophobic pockets within the protein structure.[10,122]

The HaloTag technique was recently utilized primarily by the team of X. Zhang, by insertion of a chloroalkene group at position R_3 (Fig. 15a).[123] They initially developed the highly emissive dye **39**, which enabled the *in vitro* detection of α-synuclein aggregates and mutant superoxide dismutase 1 (SOD1).[10] The dye exhibited weak fluorescence in water but became fluorescent in glycerol at 25 °C, with a $\Phi_f \sim 22\%$. Upon lowering the glycerol temperature to −80 °C, the Φ_f increased to 33%, attributed to enhanced viscosity—from 927 cP to 3×10^{11} cP—which further suppressed non-radiative decay pathways.[89] In the case of α-synuclein fibril detection, dye **39** revealed a three-step fluorescence enhancement process: formation of soluble oligomers (weak fluorescence), growth of amyloid fibers (increased emission), and fiber maturation (brightest fluorescence). This progressive fluorescence pattern contrasts with the two-step increase observed using Thioflavin T (ThT), a commonly used probe for fibril formation (Fig. 15b).[10] To monitor the aggregation of a protein of interest in live cells, Zhang and co-workers employed the HaloTag technique in combination with synthetic dyes. In this strategy, dyes were functionalized with a chloroalkene group at the R_3 position to enable bioconjugation with HaloTag (Fig. 15a). Importantly, the spectral properties of the dyes remained largely unchanged upon introduction of the chloroalkene functionality. Dye **39a** was inspired from dye **39** to introduce two hydroxyl groups for a better water solubility and a chlorohexane for the protein conjugation (Halo-tag).[10] The aggregation of fused protein ($\lambda_{ex}/\lambda_{em}$ = 530/630 nm) with SOD1(V31A) mutant resulted in a remarkable increase in Φ_f of dye **39a** up to 22%, which was observed in both vitro and vivo. The strategy was also conducted to visualize the distinct aggregation process of huntingtin exon 1 protein (Htt) mutants with varied length of polyglutamine repeats in cells. Compared to no fluorescence appearing in proteins with short glutamine repeats (Htt-16Q), the moderate length Htt-Q46 led to diffused fluorescence in the cytosol, whereas Htt-97Q containing longer glutamine repeats activated the fluorescence of dye **39a** upon the formation of granular structures.

However, using a single fluorophore typically allows visualization of only one state of protein aggregation *via* turn-on fluorescence in cells. To overcome this limitation, several pairs of imidazolinone-based fluorophores were developed for dual-color imaging, enabling the distinction of multiple aggregation stages through different emission colors—such as misfolded soluble oligomers and insoluble aggregates. Zhang and coworkers found that the viscosity sensitivity of these fluorophores strongly depended on substitutions at the R_1 and R_2 positions.[89] Based on that, dye **40** ($\lambda_{ex}/\lambda_{em}$ = 450/518 nm) was designed to become fluorescent only under high-viscosity conditions. It was subsequently modified to form dye **40a** ($\lambda_{ex}/\lambda_{em}$ = 450/520 nm) for dual-color imaging in combination with dye **39a** ($\lambda_{ex}/\lambda_{em}$ = 540/640 nm). During SOD1-A4V protein aggregation, red emission from dye **39a** was observed in diffusive and small granular structures throughout the aggregation process, while green fluorescence from dye **40a** appeared only upon formation of stationary aggregates (Fig. 15c). Alternatively, red-shifted probes were created by extending the π-conjugated bridge, such as dye **41**, which emitted at 630 nm (λ_{abs} = 485 nm). Its derivative, dye **41a**, was also used in combination with dye **40a** to monitor multistep protein aggregation. Additionally, introducing hydrogen bonding groups modulate the viscosity sensitivity of RBFs.[69] Guided by this principle, Zhang *et al.* developed *o*-HBDI derivatives **42** and **43** with tunable sensitivity for dual-color imaging.[69] Notably, dye **42** is more red-shifted ($\lambda_{ex}/\lambda_{em}$ = 580/670 nm), reducing spectral overlap with dye **43** ($\lambda_{ex}/\lambda_{em}$ = 470/510 nm).

In addition to HaloTag technique, the multiple reactive residues of proteins also provide great opportunities to directly react with functional groups of dyes. The main concern of this strategy is the reaction efficiency. Wang *et al.* developed dye **44** containing an epoxide warhead as the covalent ligand for detecting protein aggregation in the cardiac proteome (Fig. 15a).[122]

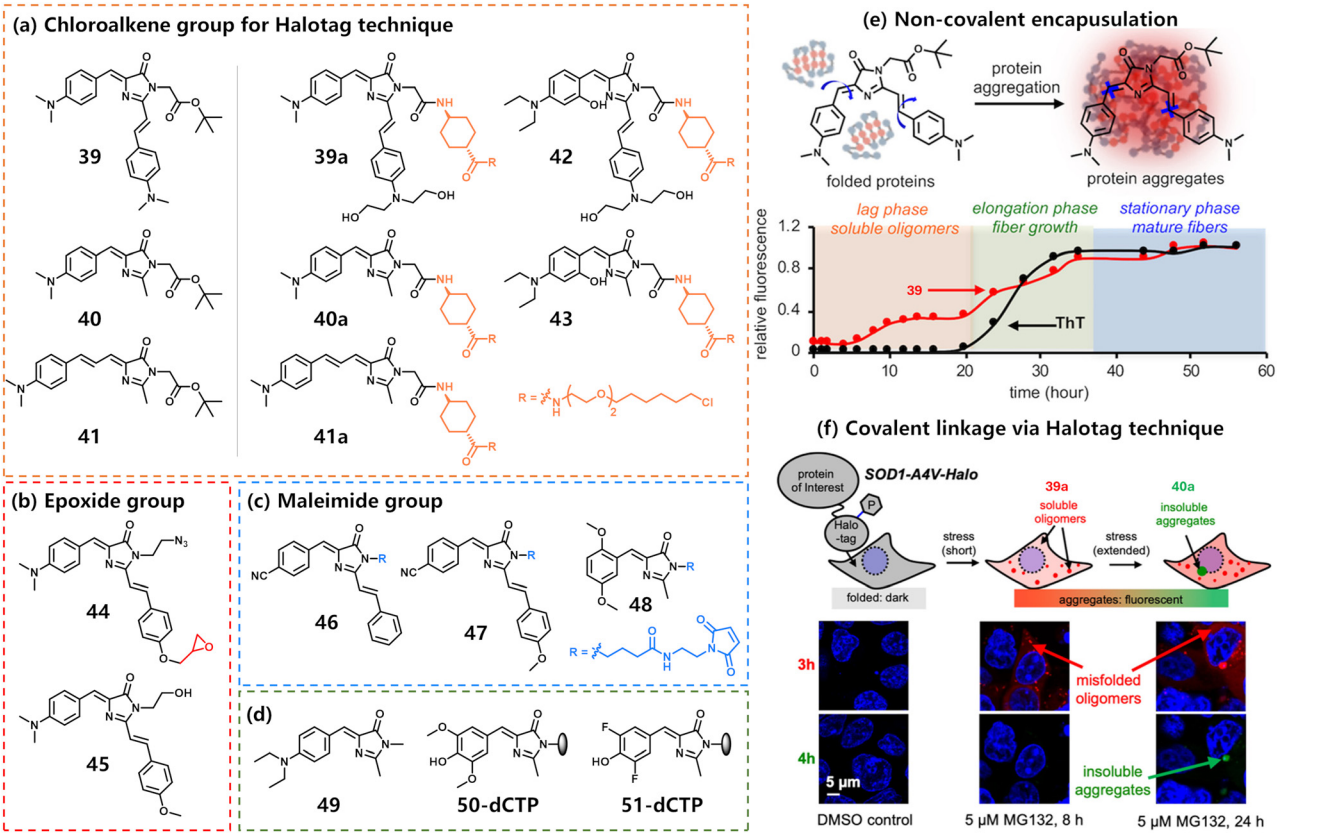

Fig. 15 Imidazolinone-based dyes encapsulated in protein matrixes. Chemical structure of dyes for the protein imaging and sensing, including (a) chloroalkene-modified imidazolinone-based dyes for Halotag technique (in orange box), (b) epoxide-substituted dyes for the covalent linkage on proteins (in red box), (c) maleimide-modified dyes for the reaction with cysteine residues (in blue box), and (a), (b) and (d) other dyes discussed to be confined in protein environments. (d) Dyes **50-dCTP** and **51-dCTP** are covalently linked to dCTP with a propargyl linker (grey ellipse). (e) Illustration of the fluorescence activation of dye **39** in protein aggregation and the aggregation kinetics of α-synuclein measured by dye **39** and ThT.[10] (f) The application of dye **39a** and **40a** in the dual-color imaging of SOD1-A4V aggregation in MG-132 treated cells, including the formation of misfolded oligomers and insoluble aggregates.[89,123] Copyrights 2018 and 2022 American Chemical Society. See Table 1 for detailed spectroscopic data.

The epoxide group can react with cysteine or other reactive residues of aggregated proteins rather than folded ones. Compared to noncovalent dye **45**, both dyes could detect protein aggregation with a α_f of 3.8 or 10.3, respectively. In addition, this covalent strategy led to stronger fluorescence enhancement of dye **44** in aggregated proteins (Φ_f = 29%), formed by heating in acidic aggregation buffer, than that of dye **45** (Φ_f = 16%). These results enabled dye **44** to be used for imaging stress-induced protein aggregation in cardiac cells and for detecting cardiac damage in mice. Recently, Belousov and coworkers designed two thiol reactive dyes with the 4-nitrile (dyes **46** and **47**) and 2,5-dimethoxy group (dye **48**), in which the maleimide group could react with cysteine residues of proteins.[124] All dyes showed week fluorescence in water (Φ_f < 0.7%) with emission in orange range.

Finally, Chang and coworkers discovered that amino-decorated fluorophores could act as sensors for human serum albumin (HSA), exhibiting fluorescence enhancement upon protein binding.[8] For example, the emission intensity of dye **49** (Fig. 15a) was weak in the mixed solvents of ethanol and DMSO (1 vol%), which was greatly enhanced ($\alpha_f \approx 10$) when binding to HSA. In addition, Riedl *et al.* attached dyes DMHBI (**50**) and DFHBI (**51**) to deoxycytidine triphosphate (dCTP) with a propargyl linker (Fig. 15a), which could serve as substrates for the enzymatic synthesis of DNA.[87] When the labeled DNA is bound to a protein, their fluorescence could be activated with 2–3.2 times increase.

4.5. Nucleic acids

Like proteins, nucleic acids such as RNA and DNA can act as natural scaffolds for fluorescent dyes, allowing structural conformations to be visualized. For example, dye **3** was shown to preferentially bind total RNA, exhibiting strongest fluorescence compared to that of complexes with ssDNA, dsDNA, and transfer RNA.[8]

More broadly, *p*-HBDI derivatives can display turn-on fluorescence upon binding to specific RNA or DNA aptamers (Fig. 16). These aptamers frequently adopt guanine–quadruplex (G4) structures formed by guanine-rich sequences, which, when properly folded, provide binding sites that enhance dye fluorescence.

Jaffrey and co-workers demonstrated fluorescence activation of diverse GFP-chromophore analogs through RNA binding.[95,125] Among them, DMHBI (**50**) and DFHBI (**51**) showed dramatic increases in Φ_f upon RNA binding in aqueous buffer, from < 0.1% to 6% and 72%, respectively. Notably, the Spinach aptamer

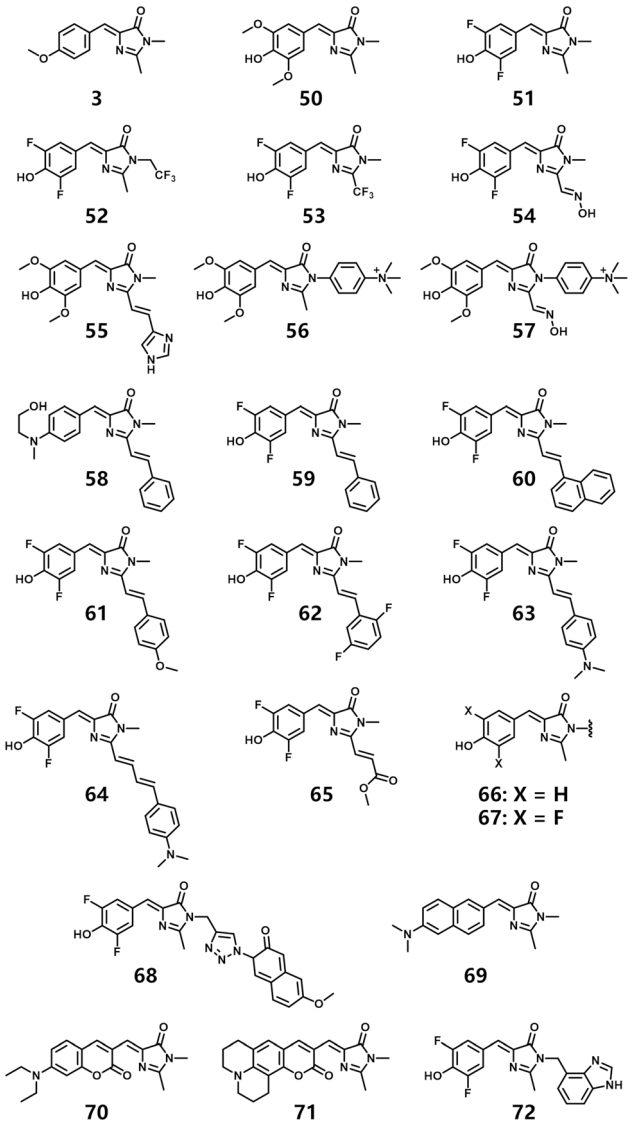

Fig. 16 Chemical structure of selected dyes confined in nucleic acids. The zigged lines indicates where the dyes are covalently linked the nucleic acids (dyes **66–67**). See Table 1 for detailed spectroscopic data.

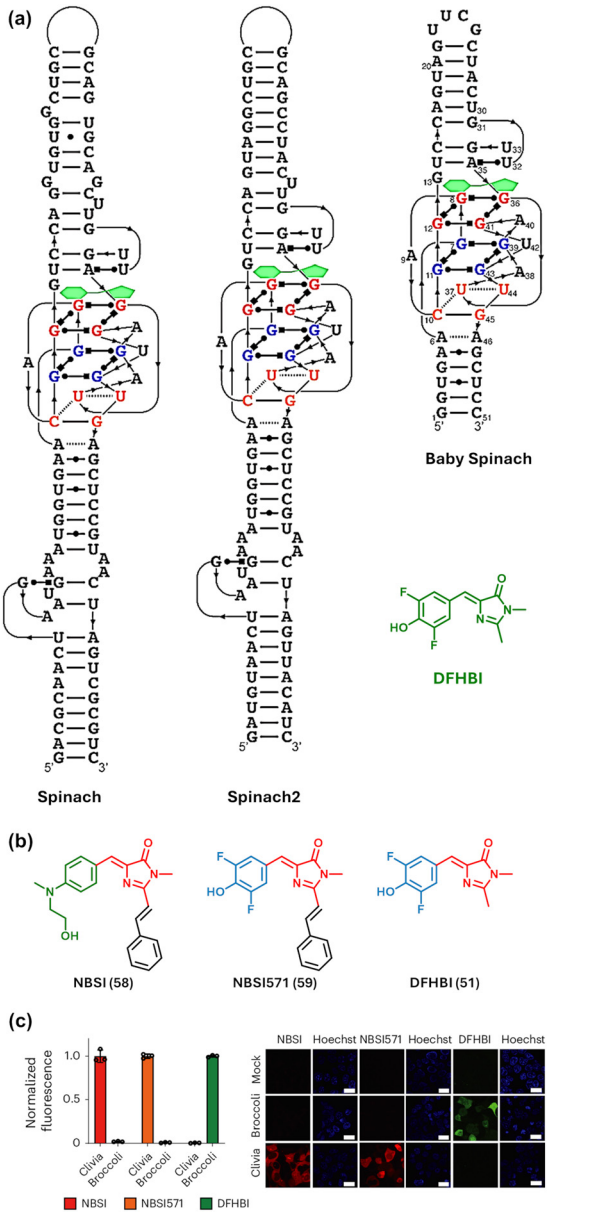

Fig. 17 Encapsulation of HBDI-dyes in RNA structures. (a) Secondary structure of Spinach, Spinach2, and Baby Spinach with the fluorophore DFHBI (**51**) stabilized on the top of the G-quadruplex structure.[125] Copyright 2016 Frontiers. (b) Chemical structures of NBSI (**58**), NBSI571 (**59**), and DFHBI (**51**), and (c) fluorescence assay of the Clivia and Broccoli aptamers binding to three dyes *in vitro* and in HEK293T cells.[130] Scale bars: 20 μm. Copyright Nature Publishing group 2024. See Table 1 for detailed spectroscopic data.

(Fig. 17a), in complex with DFHBI, was the first system to mimic EGFP by emitting bright green fluorescence ($\lambda_{ex}/\lambda_{em}$ = 469/501 nm). Compared with GFP, the Spinach aptamer showed greater photostability and enabled rapid fluorescence detection, with a dissociation constant (K_d) of 537 nM. However, its limited folding efficiency reduced fluorescence activation in cells. This limitation was addressed by the development of Spinach2 (Fig. 17a), which folded more reliably while retaining nearly identical spectral properties ($\lambda_{ex}/\lambda_{em}$ = 447/501 nm) and a comparable K_d (~530 nM).[126] Further modifications produced DFHBI-1T (**52**) and DFHBI-2T (**53**), which form complexes with Spinach2 and exhibit red-shifted excitation/emission maxima at 482/505 nm and 500/523 nm, respectively, making them better suited for existing imaging instrumentation.[127] These studies also highlighted the critical role of the G-quadruplex motif in Spinach fluorescence, which inspired the design of "Baby Spinach", a minimized aptamer that still binds DFHBI effectively (Fig. 17a).[80] Moreover, Kikuchi and Kolpashchikov engineered a split Spinach aptamer, in which two fragments were connected by an analyte-binding module complementary to RNA or DNA targets.[128] Upon hybridization with the correct analyte, the probe restored DFHBI fluorescence with quantum yield enhancement up to 270-fold, achieving high selectivity for nucleic acid detection under physiological conditions.

After the Spinach family, Jaffrey and coworkers developed other RNA–fluorophore complexes, including Broccoli,[96,129]

and Corn.[96] Broccoli was explored through the SELEX (Systematic Evolution of Ligands by Exponential Enrichment) protocol, showing fast folding to activate green fluorescence of DFHBI-IT ($\lambda_{ex}/\lambda_{em}$ = 469/507 nm) in cells.[129] Furthermore, Corn was developed with the combination of dye DFHO (**54**) for the quantitative measurement of transcript-level imaging in live cells.[96] In comparison to the complexation with orange or red Broccoli, the Corn-DFHO complexes exhibited outstanding photostability and lowest K_d at 70 nM.

Additionally, fluorogenic RNA–fluorophore complexes with a large Stokes shift possess promising advantages for bioimaging. Höbartner and coworkers invented a RNA aptamer, named Chili, to induce high Stokes shifts (>100 nm) of several HBDI derivates, including DMHBI (**50**, $\lambda_{ex}/\lambda_{em}$ = 400/537 nm), DMHBI-Imi (**55**, $\lambda_{ex}/\lambda_{em}$ = 463/545, 594 nm), DMHBI$^+$ (**56**, $\lambda_{ex}/\lambda_{em}$ = 413/542 nm), and DMHBO$^+$ (**57**, $\lambda_{ex}/\lambda_{em}$ = 456/592 nm).[81] Compared to DMHBI and DMHBI-Imi, the trimethylammonium-substituted phenyl ring of DMHBI$^+$ at position R_3 facilitated the binding with RNA through the stacking interactions with nucleobases and the electrostatic interactions with the polyphosphates. A low-nanomolar affinity was observed for Chili-DMHBI$^+$ complexes with a K_d of 63 nM. Afterwards, DMHBO$^+$ was designed to bind with Chili as a mimic of RFP for orange-red emission. Recently, Huang *et al.* suggested the fluorescence activation of NBSI (**58**) and its derivates using the small and monomeric Clivia aptamer (Fig. 17b).[130,131] The Clivia–NBSI complex exhibited stable fluorescence ($\lambda_{ex}/\lambda_{em}$ = 524/580 nm) with a low K_d of 55 nM. Given to previous investigations, NBSI and its derivates were designed with a dialkylamino group to increase the electron-donating ability and a styryl group to increase the intramolecular charge transfer, resulting in a high Stoke shifts.[131] The modification on the styryl group led to the emission wavelengths of complexes with Clivia varying from 570 to 624 nm. Among them, NBSI571 (**59**) exhibited a lower binding affinity but displayed the largest Stokes shift, reaching 108 nm.[131] Compared to Chili-labeled RNAs, the utilization of Clivia and NBSI-based dyes enabled to tag and image small non-coding RNAs in live cells. These Clivia–fluorophore complexes have been employed orthogonally with other fluorogenic Pepper[131] or Broccoli[130] for dual-color imaging benefiting from the specific recognition between RNAs and dyes. For example, the binding affinity of NBSI or NBSI571 to Clivia was obviously stronger than Broccoli, while DFHBI reversely preferred Broccoli (Fig. 17c). As a result, the complexes of Clivia with NBSI or NBSI571 emitted bright red light within HEK293T cells, whereas the Broccoli-DFHBI complex could only be seen in green channel.

Similarly, G-quadruplex formed by DNA has also been exploited. Feng and coworkers developed a RFP-like system (λ_{em} = 583–668 nm) based on DNA G4s.[99] The parallel-to-antiparallel transformation of the DNA structure induced by the addition Pb^{2+} and EDTA could trigger the on–off fluorescence of DNA G4 (NG16) and dye **62** complexes. The emission of synthetic RFP chromophore analogs (dyes **59–64**) in the red and far-red regions was enhanced by strong π–π stacking with NG16 with K_d of ∼2 μM except for dye **65** (K_d = 24.88 μM). The quantum yields of the free fluorophores were below 0.7% in aqueous solutions at pH 8, while NG16-flurophroe complexes showed remarkably enhanced values (Φ_f = 3.2%), with the exception of dye **65**. These complexes also exhibited large Stokes shift up to 121 nm. For imaging purposes, a specific probe was prepared with the introduction of a reporter part of two NG16-**62** complexes and a recognition segment sgc8 to target a cancer-related protein tyrosine kinase-7 (PTK7) on cell membranes. The DNA fluorescent probe was proved for a long-term real-time imaging of living tumor cells with high PTK7 expression, due to its high quantum yield, large Stokes shifts, and good photostability. This probe was also utilized in bioimaging of tissues, benefiting from its two-photon absorption properties.

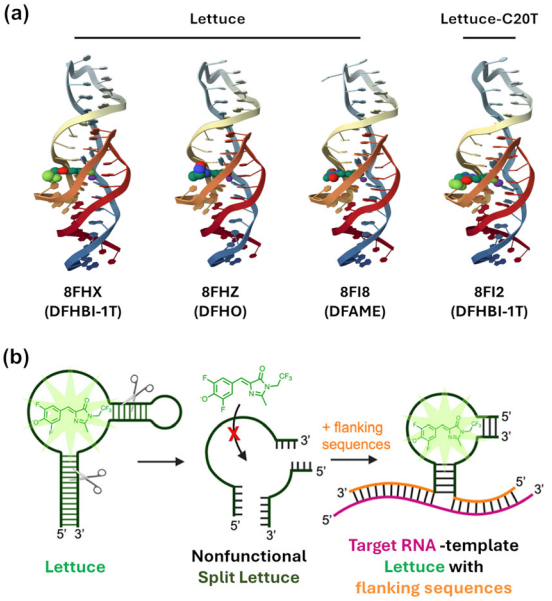

Fig. 18 Lettuce-dye complexes. (a) Structure of Lettuce-dye complexes. Shown are complexes structures, aptamer type, dye name and PDB identifiers for Lettuce-DFHBI-1T (8FHX), Lettuce-DFHO (8FHZ), Lettuce-DFAME (8FI8), and Lettuce-C20T-DFHBI-1T (8FI2). The structural information was acquired from Protein Data Bank (PDB). (b) Illustration of RNA detection using split Lettuce with DFHBI-1T (**52**).[100] Copyright 2022 American Chemical Society. See Table 1 for detailed spectroscopic data.

Moreover, Jaffrey and coworkers developed Lettuce, a fluorogenic DNA aptamer, by binding DFHBI-1T (**52**) with a K_d of 350 nM (Fig. 18a).[82,100] The fluorescence emission of Lettuce-DFHBI-1T complex ($\lambda_{ex}/\lambda_{em}$ = 455/505 nm) was higher compared to that of free dye with α_f around 11.[100] Interestingly, Lettuce can be divided into two nonfluorescent separated oligonucleotides, which became fluorescent when their proximity was induced by a target RNA (Fig. 18b). Due to this property, the modified split Lettuce with a complementary part for targeting to SARS-CoV-2 RNA led to effectively detect viral RNA by the turn-on fluorescence. Furthermore, Lettuce and its mutants on residue 20 were extensively studied with the complexation of DFHBI-1T (**52**), DFHO (**54**), and DFAME (**65**) (Fig. 18a).[82] Among these DNAs, the C20T mutant could activate DFHBI-1T with nearly same emission intensity to the wild-type Lettuce, while it could slightly enhanced the fluorescence of DFAME and led to a nearly double intensity of DFHO.

In addition to DNA G4s, the formation of DNA triplexes has also been demonstrated to enhance the emission of DNA-embedded fluorophores by Seio and coworkers.[88] They synthesized uridine-based precursors functionalized with dyes **66** and **67** for the preparation of fluorescent oligodeoxynucleotides (ODNs). In the presence of triplex-forming oligodeoxynucleotides, both dye-labeled ODNs showed fluorescence enhancement with α_f values of 5.8 and 1.8 for dyes **66** and **67**, respectively.

In complex biological environments, relying solely on changes in fluorescence intensity from single-emission fluorophores can be unreliable, as various environmental factors—such as salt concentration, collisional quenching, and vibrational energy losses to water molecules—can significantly affect signal output. To address these limitations, ratiometric fluorescent probes, which emit at two distinct wavelengths, are preferred for their enhanced robustness and internal signal normalization. Leveraging the rotational properties of *p*-HBDI, researchers have developed ratiometric probes by incorporating a second environmentally insensitive dye. This design provides a more reliable and accurate approach for ratiometric sensing and imaging in biologically complex settings.[91,98] For instance, Duan and coworkers introduced the triazolyl-coumarin module onto the R_3 position of DFHBI by azide–alkyne cycloaddition.[91] The achieved fluorophore DFHBI-CM (**68**, Fig. 16) showed two independent absorption peaks at 347 nm for triazolyl-coumarin and 422 nm for DFHBI. Upon complexation with an RNA aptamer (*e.g.*, Spinach 2), the complex exhibited enhanced fluorescence at 502 nm of the sensitive DFHBI (λ_{ex} = 447 nm), while its fluorescence intensity at 420 nm from coumarin (λ_{ex} = 337 nm) remained unchanged. Therefore, the emission intensities at 502 and 420 nm was significantly determined by the RNA aptamer, which was utilized for the ratiometric detection of RNA synthesis. In addition, the coumarin molecules could be integrated into the conjugated structure of imidazolinone-based fluorophores (dyes **69–71**, Fig. 16) as sensors for the detection of DNA G4s with dual fluorescence emission.[98] Similarly, the inherent fluorescence of the coumarin structure was stable before and after the addition of G4 ($\lambda_{ex}/\lambda_{em}$ = 399/490 nm). The emission of whole HDBI-based fluorophore was gradually enhanced at the wavelength of 613 nm (λ_{ex} = 560 nm). Referring to the restrictions on the imidazolinone-based fluorophore, the intensity could be improved up to 52-fold when adding the G4 from 1 μL to 10 μL. The integrated fluorophore has been utilized to distinguish cell apoptosis and ferroptosis by tracking G4s using green emission of the coumarin as the internal reference signal.

In addition to the rational design of dyes, Jaffrey and coworker also reported an RNA-based ratiometric sensor for the metabolite imaging.[93] They first demonstrated that the Squash, a *S*-adenosylmethionine (SAM)-binding aptamer, could trigger the fluorescence enhancement of synthetic fluorophores DFHBI-1T and DFHO with higher Φ_f values of 71% and 60% in HEPES buffer, respectively. The ratiometric sensor was then designed with the composition of Broccoli binding with BI (**72**)[97] in one arm and Squash in the other arm. The Broccoli-BI complex provided signal normalization ($\lambda_{ex}/\lambda_{em}$ = 460/500 nm) and the Squash-DFHO complex exhibited dynamic emission intensity ($\lambda_{ex}/\lambda_{em}$ = 512/575 nm) in ratio to SAM levels. As the result, the orange to green fluorescence ratio achieved from the sensor was used to quantitatively measure SAM and reveal its metabolic origins.

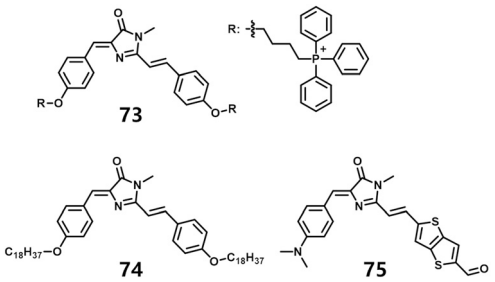

Fig. 19 Chemical structure of selected dyes confined in cellular environments. See Table 1 for detailed spectroscopic data.

4.6. Cellular environments

The strong affinity of these various fluorophores for hydrophobic regions of amphiphilic bio(macro)molecules and its molecular rotor nature has naturally been exploited in biological imaging.

A phosphonium-modified dye **73** was developed for the detection of mitochondrial viscosity in live cells (Fig. 19).[132] The dye exhibits high sensitivity to viscosity changes, responding across a wide range (7.9 cP to 438.4 cP), which is attributed to restricted rotation of both single bonds and excited-state C=C double bonds. Fluorescence enhancement under increased viscosity is particularly notable, as the dye's molar absorptivity significantly increases with viscosity. A proof-of-concept experiment demonstrated the monitoring of mitochondrial viscosity during HeLa cell apoptosis. Incorporation of long hydrophobic alkyl chains into the fluorophore structure facilitated membrane and endoplasmic reticulum insertion, as demonstrated with dye **74** (Fig. 19) in live HeLa, CHO, A549, and 7901 cells.[94]

Recently, Zhang *et al.* developed a near-infrared dye (**75**), analogous to the GFP chromophore, capable of dual detection of cysteine and viscosity.[133] Fluorescence is quenched upon reaction with cysteine but enhanced in viscous environments, allowing independent measurement of both factors. In HeLa cells, the dye shows weak emission in the presence of cysteine, strong emission in high-viscosity regions, and remarkably intense fluorescence when both conditions coexist, demonstrating its dual-sensing capability.

These findings highlight the potential of supramolecular confinement strategies to modulate the photophysical and chemical reactivity of GFP-like chromophores outside of a protein scaffold.

5. Applications

Rational molecular design of imidazolinone-based dyes, combined with their integration into diverse matrix systems, enables precise modulation of key photophysical properties—including photostability, excitation/emission profiles, quantum yield, viscosity sensitivity, and brightness. This versatility has

driven their adoption in imaging and sensing, where tunable fluorescence responses (''on–off'' switching) allow for the development of environment-sensitive smart materials. Beyond these applications, their light-harvesting capabilities have been exploited in phototherapy, photocatalysis, and optoelectronic devices. The applications for each dye are provided in Table 1 and detailed thereafter.

5.1. Bioimaging and biosensing

A major challenge for most fluorescent dyes used in biological environments is their poor water solubility. While the parent dye *p*-HBDI exhibits reasonable solubility at physiological pH, this is not the case for rigidified, lipophilic or halogenated derivatives. This limitation restricts their use in monitoring biological activities, even when solubilized in minimal DMSO concentrations, due to potential cytotoxicity—particularly at high doses or prolonged incubation times.[90,134–136] Hydrophilic modifications, such as carboxyl groups (*e.g.*, dye **6**),[92] are rarely reported, leaving DMSO as the default solvent for cell-based assays.

Despite these constraints, imidazolinone dyes have been functionalized for targeted bioimaging applications.[137] Their tunable fluorescence with polarity, viscosity or lipophilic properties enables localization in specific cellular compartments (*e.g.*, membranes,[92] endoplasmic reticulum,[94] mitochondria,[132] and lysosomes[138]) and viscosity-sensitive detection of processes like apoptosis.[132] The ''on–off'' fluorescence mechanism has also been harnessed for *in vitro*/*in vivo* detection of metal ions,[60] HSA[8] and cysteine,[64,133] as well as for visualizing latent fingerprints *via* ammonium-functionalized dyes that target fatty acids,[121] and for revealing the triplex-forming oligodeoxynucleotides using dye-labeled precursors.[88]

An alternative strategy for water-based applications, involves integrating dyes into biocompatible materials as fluorescent probes through non-covalent encapsulation or covalent linkage. Dyes are mostly employed in water-dispersible matrix systems (*e.g.*, MOF, RNA, DNA, proteins, or polymers), which not only resolves solubility issues but also enhances photophysical properties (*e.g.*, photostability, emission wavelength). For example, RNA/DNA–dye complexes – including various RNA aptamers (*e.g.*, Spinach, Broccoli, Corn, Chili, and Civia),[80,95,96,126,127,129–131,139] DNA G-quadruplex (*e.g.* NG16, Lettuce),[82,99,100] and dsDNA[87] – enable green-to-red and near-infrared imaging. These systems serve as fluorogenic probes for live-cell analysis and biosensing applications, including SARS-CoV-2 RNA targeting,[100] RNA synthesis monitoring,[91] and DNA–protein interaction studies.[87] In protein–fluorophore systems (*e.g.*, HaloTag-based GFP mimics)[123] they facilitate real-time visualization of disease-relevant protein behaviors such as aggregation.[10,61,69,89,122] Furthermore, MOF–dye systems have enabled cytoplasmic staining,[83] whereas dye-labeled amphiphilic copolymers form tunable assemblies in aqueous solution that enable multicolor cell imaging with single-excitation precision.[84,112–114,116]

Finally, some groups describe the two-photon absorption and excitation with imidazolinone derivatives,[52,74,75,116,140] which holds significant potentials in two-photon imaging in cells and tissues by improving the penetration of light.[99,131,138,141]

5.3. Phototherapy

Reactive oxygen species (ROS)[142] play a pivotal role in phototherapy, particularly in photodynamic therapy (PDT), where they induce targeted cellular damage. Li *et al.* developed an imidazolinone-based photosensitizer designed for PDT and bioimaging, incorporating an anthracene group to generate singlet oxygen and a morpholine moiety to target lysosomes, thereby enhancing therapeutic efficacy.[138] This dye, with absorption/emission maxima at 450/610 nm and a singlet oxygen quantum yield of 21%, demonstrated efficient uptake in tumor cells and zebrafish, achieving lysosome-specific localization and apoptosis induction. In parallel, Liu *et al.* explored KillerRed chromophore analogs—synthetic GFP derivatives with extended conjugation—to generate ROS for PDT and chromophore-assisted light inactivation (CALI).[65,143] These dyes, leveraging their high protein-binding affinity, enabled profiling of protein aggregate interactomes while serving as potent photosensitizers for therapeutic applications.

5.4. Others

Beyond biosensing, imidazolinone-based dyes have been used to detect Hg^{2+} ions[105] and has been integrated into microporous cavities for the detection of nitroaromatic pollutants and explosives.[111] Such examples demonstrate their versatility in non-biological sensing applications.

These synthetic dyes and their bioinspired systems have also been adapted for other light-driven fields, including photocatalysis, optoelectronic devices, optical waveguiding, fluorescent ink, and fluorescence anti-counterfeiting.

For instance, Maji *et al.* developed a conjugated microporous polymer incorporating dye **22** coupled with triphenylamine, designed for bioinspired photocatalytic CO_2 reduction to CO.[110] In this system, triphenylamine functions as both a photon antenna and electron donor, leading to improved CO production and selectivity compared to donor-free materials. This enhancement is attributed to superior light-harvesting, charge separation, and migration capabilities.

Additionally, Chou and coworkers utilized a locked dye (*o*-LHBDI) to fabricate OLEDs, amplifying spontaneous emission and enabling the emission of narrow monochromatic light.[46] Gonnade *et al.* explored the single crystal and cocrystal approach to fabric luminescent materials based on imidazolinone-based dyes for both 1D and 2D optical waveguiding.[106,107] Among them, dye **11** and **12** has been mixed with polyvinyl alcohol to serve as fluorescent inks as well as security inks for anti-counterfeiting capacities by inducing the thermoresponsive transformation of dye crystals. Furthermore, the application of the fluorescence anti-counterfeiting have also been achieved by tuning the binding abilities between dye **33** and CB[7].[117] These innovative applications underscore the broad potential of imidazolinone-based fluorophores across diverse optical technologies.

6. Conclusion and perspectives

This review highlights the most recent and promising progress in the development of chemically synthesized GFP-inspired fluorescent systems. The unique emission properties of GFP arise from the interplay of ESPT and the confinement of the protein cage, which suppresses non-radiative decays through TICT. Inspired by these basic principles, new fluorescent proteins have been generated through mutations in the chromophore-forming tripeptide or the surrounding protein environment, while purely chemical approaches have yielded imidazolinone-based dyes synthesized *via* the Erlenmeyer azlactone method, Knoevenagel condensation, and [2 + 3] cycloaddition. By tailoring electron-donating or electron-withdrawing substituents, restricting intramolecular motion, and designing ratiometric probes, researchers have broadened the photophysical versatility of these synthetic fluorophores.

One step closer to materials, multiple confinement strategies have been developed to mimic the protein cage and stabilize synthetic dyes within rigid cavities or macromolecular backbones. Such approaches have enabled new functional platforms for imaging, sensing, phototherapy, and photocatalysis. Substrate choice is driven largely by the need to restrict fluorophore motion while ensuring biocompatibility. Although biological scaffolds such as viruses, RNA, and DNA provide excellent confinement, their limited yields constrain scalability. By contrast, biocompatible polymers, including polypeptides, polyesters, and polysaccharides, offer promising alternatives, combining high-yield production with structural diversity for engineering functional fluorescent materials.

Despite these advances, significant challenges remain. The fluorescence efficiencies (Φ_f) of most synthetic imidazolinone dyes are still below those of natural GFP, even when confined. Only a few RNA-binding analogs approach the brightness of wild-type GFP, yet they still lag behind evolved variants such as enhanced GFP (EGFP). Moreover, most synthetic dyes emit in the blue-yellow spectral range, with limited progress toward red or near-infrared emitters that are essential for advanced bioimaging. Overcoming these limitations will require synthetic strategies that couple high quantum yields with red-shifted emission and robust photostability.

Looking forward, the design of next-generation GFP-inspired systems will benefit from a convergence of synthetic chemistry, materials science, and bioengineering. Achieving scalable, biocompatible, and red/NIR-emissive platforms will be crucial for translating confined fluorophores into real-world biomedical and photonic applications. Importantly, these artificial GFP-like systems should not only aim to replicate natural proteins but also push beyond them, enabling entirely new classes of multifunctional photoactive materials for sensing, biocatalysis, and therapy.

Author contributions

S. Ji: visualisation, writing – original draft. S. Lecommandoux: conceptualization, funding acquisition, supervision, writing – review & editing. C. Bonduelle: conceptualization, funding acquisition, supervision, writing – original draft. C. Grazon: conceptualization, supervision, validation, writing – original draft.

Conflicts of interest

There are no conflicts to declare.

Data availability

No primary research results, software or code have been included and no new data were generated or analysed as part of this review.

Acknowledgements

This work was supported by China Scholarship Council (202008320295) for Sifan Ji and by a grant overseen by the French National Research Agency (ANR, Grant No. ANR-23-CE09-0006). Continuous support from CNRS, Université de Bordeaux and Bordeaux-INP is greatly acknowledged.

References

1 S. Duwe and P. Dedecker, *Curr. Opin. Biotechnol*, 2019, **58**, 183–191.
2 O. Shimomura, F. H. Johnson and Y. Saiga, *J. Cell. Comp. Physiol.*, 1962, **59**, 223–239.
3 M. Chalfie, Y. Tu, G. Euskirchen, W. W. Ward and D. C. Prasher, *Science*, 1994, **263**, 802–805.
4 G. S. Baird, D. A. Zacharias and R. Y. Tsien, *Proc. Natl. Acad. Sci. U. S. A.*, 2000, **97**, 11984–11989.
5 M. Ormo, A. B. Cubitt, K. Kallio, L. A. Gross, R. Y. Tsien and S. J. Remington, *Science*, 1996, **273**, 1392–1395.
6 A. A. Pakhomov and V. I. Martynov, *Chem. Biol.*, 2008, **15**, 755–764.
7 D. M. Chudakov, M. V. Matz, S. Lukyanov and K. A. Lukyanov, *Physiol. Rev.*, 2010, **90**, 1103–1163.
8 J. S. Lee, A. Baldridge, S. Feng, Y. SiQiang, Y. K. Kim, L. M. Tolbert and Y. T. Chang, *ACS Comb. Sci.*, 2011, **13**, 32–38.
9 A. Follenius-Wund, M. Bourotte, M. Schmitt, F. Iyice, H. Lami, J. J. Bourguignon, J. Haiech and C. Pigault, *Biophys. J.*, 2003, **85**, 1839–1850.
10 Y. Liu, C. H. Wolstenholme, G. C. Carter, H. Liu, H. Hu, L. S. Grainger, K. Miao, M. Fares, C. A. Hoelzel, H. P. Yennawar, G. Ning, M. Du, L. Bai, X. Li and X. Zhang, *J. Am. Chem. Soc.*, 2018, **140**, 7381–7384.
11 E. A. Dolgopolova, A. M. Rice, M. D. Smith and N. B. Shustova, *Inorg. Chem.*, 2016, **55**, 7257–7264.
12 H. Deng and X. Zhu, *Mater. Chem. Front.*, 2017, **1**, 619–629.
13 O. Shimomura, *FEBS Lett.*, 1979, **104**, 220–222.
14 C. W. Cody, D. C. Prasher, W. M. Westler, F. G. Prendergast and W. W. Ward, *Biochemistry*, 1993, **32**, 1212–1218.

15 R. Heim, D. C. Prasher and R. Y. Tsien, *Proc. Natl. Acad. Sci. U. S. A.*, 1994, **91**, 12501–12504.
16 B. G. Reid and G. C. Flynn, *Biochemistry*, 1997, **36**, 6786–6791.
17 R. Y. Tsien, *Annu. Rev. Biochem.*, 1998, **67**, 509–544.
18 H. Niwa, S. Inouye, T. Hirano, T. Matsuno, S. Kojima, M. Kubota, M. Ohashi and F. I. Tsuji, *Proc. Natl. Acad. Sci. U. S. A.*, 1996, **93**, 13617–13622.
19 G. Jung, C. Bräuchle and A. Zumbusch, *J. Chem. Phys.*, 2001, **114**, 3149–3156.
20 S. P. Laptenok, J. Conyard, P. C. Page, Y. Chan, M. You, S. R. Jaffrey and S. R. Meech, *Chem. Sci.*, 2016, **7**, 5747–5752.
21 A. P. Demchenko, *BBA Adv.*, 2023, **3**, 100085.
22 S. R. Meech, *Chem. Soc. Rev.*, 2009, **38**, 2922–2934.
23 X. He, A. F. Bell and P. J. Tonge, *FEBS Lett.*, 2003, **549**, 35–38.
24 M. Andresen, M. C. Wahl, A. C. Stiel, F. Grater, L. V. Schafer, S. Trowitzsch, G. Weber, C. Eggeling, H. Grubmuller, S. W. Hell and S. Jakobs, *Proc. Natl. Acad. Sci. U. S. A.*, 2005, **102**, 13070–13074.
25 S. L. Maddalo and M. Zimmer, *Photochem. Photobiol.*, 2007, **82**, 367–372.
26 R. S. Liu, *Acc. Chem. Res.*, 2001, **34**, 555–562.
27 S. Mukherjee and R. Jimenez, *J. Phys. Chem. B*, 2022, **126**, 735–750.
28 R. M. Wachter, B. A. King, R. Heim, K. Kallio, R. Y. Tsien, S. G. Boxer and S. J. Remington, *Biochemistry*, 1997, **36**, 9759–9765.
29 R. M. Wachter, M.-A. Elsliger, K. Kallio, G. T. Hanson and S. J. Remington, *Structure*, 1998, **6**, 1267–1277.
30 M. V. Matz, A. F. Fradkov, Y. A. Labas, A. P. Savitsky, A. G. Zaraisky, M. L. Markelov and S. A. Lukyanov, *Nat. Biotechnol.*, 1999, **17**, 969–973.
31 M. Wang, Y. Da and Y. Tian, *Chem. Soc. Rev.*, 2023, **52**, 1189–1214.
32 A. Miyawaki and Y. Niino, *Mol. Cell*, 2015, **58**, 632–643.
33 J. Kong, Y. Wang, W. Qi, M. Huang, R. Su and Z. He, *Adv. Colloid Interface Sci.*, 2020, **285**, 102286.
34 M. S. Tsai, C. L. Ou, C. J. Tsai, Y. C. Huang, Y. C. Cheng, S. S. Sun and J. S. Yang, *J. Org. Chem.*, 2017, **82**, 8031–8039.
35 H. Deng, C. Yu, L. Gong and X. Zhu, *J. Phys. Chem. Lett.*, 2016, **7**, 2935–2944.
36 S. Kojima, H. Ohkawa, T. Hirano, S. Maki, H. Niwa, M. Ohashi, S. Inouye and F. I. Tsuji, *Tetrahedron Lett.*, 1998, **39**, 5239–5242.
37 S. M. H. Sanad and A. E. M. Mekky, *J. Heterocycl. Chem.*, 2020, **57**, 3930–3942.
38 M. El-Araby, A. Omar, H. H. Hassanein, A. G. El-Helby and A. A. Abdel-Rahman, *Molecules*, 2012, **17**, 12262–12275.
39 B. K. Rajbongshi, N. N. Nair, M. Nethaji and G. Ramanathan, *Cryst. Growth Des.*, 2012, **12**, 1823–1829.
40 L. Bischoff, C. Hoarau, M. Museli, L. Colombeau and J. Hédouin, *Synlett*, 2016, 2819–2825.
41 V. G. Rajurkar, S. J. Shinde and V. K. Deshmukh, *Anal. Chem. Lett.*, 2018, **8**, 578–586.
42 C.-Y. Lee, Y.-C. Chen, H.-C. Lin, Y. Jhong, C.-W. Chang, C.-H. Tsai, C.-L. Kao and T.-C. Chien, *Tetrahedron*, 2012, **68**, 5898–5907.
43 H. Takeuchi, S. Hagiwara and S. Eguchi, *Tetrahedron*, 1989, **45**, 6375–6386.
44 L. Wu and K. Burgess, *J. Am. Chem. Soc.*, 2008, **130**, 4089–4096.
45 A. Baldridge, K. M. Solntsev, C. Song, T. Tanioka, J. Kowalik, K. Hardcastle and L. M. Tolbert, *Chem. Commun.*, 2010, **46**, 5686–5688.
46 Y. H. Hsu, Y. A. Chen, H. W. Tseng, Z. Zhang, J. Y. Shen, W. T. Chuang, T. C. Lin, C. S. Lee, W. Y. Hung, B. C. Hong, S. H. Liu and P. T. Chou, *J. Am. Chem. Soc.*, 2014, **136**, 11805–11812.
47 D. S. Treitler and S. Leung, *J. Org. Chem.*, 2022, **87**, 11293–11295.
48 J. M. Lerestif, J. P. Bazureau and J. Hamelin, *Tetrahedron Lett.*, 1993, **34**, 4639–4642.
49 J. Kowalik, A. Baldridge and L. Tolbert, *Synthesis*, 2010, 2424–2436.
50 L. M. Tolbert, A. Baldridge, J. Kowalik and K. M. Solntsev, *Acc. Chem. Res.*, 2012, **45**, 171–181.
51 J. M. Lerestif, J. Perrocheau, F. Tonnard, J. P. Bazureau and J. Hamelin, *Tetrahedron*, 1995, **51**, 6757–6774.
52 T. B. Clark, M. E. Orr, D. C. Flynn and T. Goodson, *J. Phys. Chem. C*, 2011, **115**, 7331–7338.
53 C. Y. Lin and S. G. Boxer, *J. Am. Chem. Soc.*, 2020, **142**, 11032–11041.
54 M. E. Martin, F. Negri and M. Olivucci, *J. Am. Chem. Soc.*, 2004, **126**, 5452–5464.
55 J. Dong, K. M. Solntsev and L. M. Tolbert, *J. Am. Chem. Soc.*, 2006, **128**, 12038–12039.
56 I. V. Yampolsky, S. J. Remington, V. I. Martynov, V. K. Potapov, S. Lukyanov and K. A. Lukyanov, *Biochemistry*, 2005, **44**, 5788–5793.
57 N. H. List, C. M. Jones and T. J. Martinez, *Commun. Chem.*, 2024, **7**, 25.
58 J. Liu, C. Chen, A. I. Sokolov, M. S. Baranov and C. Fang, *ChemPhotoChem*, 2024, **8**, e202400037.
59 C. I. C. Esteves, I. da Silva Fonseca, J. Rocha, A. M. S. Silva and S. Guieu, *Dyes Pigm.*, 2020, **177**, 108267.
60 Y. Li, L. Shi, L. X. Qin, L. L. Qu, C. Jing, M. Lan, T. D. James and Y. T. Long, *Chem. Commun.*, 2011, **47**, 4361–4363.
61 S. Ye, H. Zhang, J. Fei, C. H. Wolstenholme and X. Zhang, *Angew. Chem., Int. Ed.*, 2021, **60**, 1339–1346.
62 X. He, A. F. Bell and P. J. Tonge, *Org. Lett.*, 2002, **4**, 1523–1526.
63 N. S. Baleeva, K. A. Myannik, I. V. Yampolsky and M. S. Baranov, *Eur. J. Org. Chem.*, 2015, 5716–5721.
64 Y. Zhou, J. Dai, J. Qi, J. Wu, Y. Huang, B. Shen, X. Zhi and Y. Fu, *Spectrochim. Acta, Part A*, 2023, **286**, 121946.
65 H. Feng, Q. Zhao, B. Zhang, H. Hu, M. Liu, K. Wu, X. Li, X. Zhang, L. Zhang and Y. Liu, *Angew. Chem., Int. Ed.*, 2023, **62**, e202215215.
66 T. P. Singh, T. J. Devi, N. P. Singh and O. M. Singh, *ChemistrySelect*, 2018, **3**, 6596–6600.

67 A. Baldridge, S. R. Samanta, N. Jayaraj, V. Ramamurthy and L. M. Tolbert, *J. Am. Chem. Soc.*, 2011, **133**, 712–715.
68 M. Paez-Perez and M. K. Kuimova, *Angew. Chem., Int. Ed.*, 2024, **63**, e202311233.
69 B. Shen, L. Liu, Y. Huang, J. Wu, H. Feng, Y. Liu, H. Huang and X. Zhang, *Aggregate*, 2023, **5**, e421.
70 S. Chatterjee and P. Karuso, *Tetrahedron Lett.*, 2016, **57**, 5197–5200.
71 C. C. Hsieh, P. T. Chou, C. W. Shih, W. T. Chuang, M. W. Chung, J. Lee and T. Joo, *J. Am. Chem. Soc.*, 2011, **133**, 2932–2943.
72 T. Chatterjee, M. Mandal, A. Das, K. Bhattacharyya, A. Datta and P. K. Mandal, *J. Phys. Chem. B*, 2016, **120**, 3503–3510.
73 S. Chatterjee, K. Ahire and P. Karuso, *J. Am. Chem. Soc.*, 2020, **142**, 738–749.
74 D. Paul, P. Sahoo, A. Sengupta, U. Tripathy and S. Chatterjee, *J. Phys. Chem. B*, 2025, **129**, 692–711.
75 D. Paul, P. Sahoo, A. K. Pradhan, P. K. Datta, A. Sengupta, U. Tripathy and S. Chatterjee, *J. Chem. Phys.*, 2025, **162**, 234308.
76 C. W. Chiu, L. L. Tsao, H. Y. Lin, Y. H. Liu, M. Raabe, C. W. Lin, Y. C. Cheng and J. S. Yang, *ChemPhotoChem*, 2025, **9**, e202400400.
77 M. S. Baranov, K. M. Solntsev, N. S. Baleeva, A. S. Mishin, S. A. Lukyanov, K. A. Lukyanov and I. V. Yampolsky, *Chemistry*, 2014, **20**, 13234–13241.
78 M. S. Baranov, K. A. Lukyanov, A. O. Borissova, J. Shamir, D. Kosenkov, L. V. Slipchenko, L. M. Tolbert, I. V. Yampolsky and K. M. Solntsev, *J. Am. Chem. Soc.*, 2012, **134**, 6025–6032.
79 H. W. Ke and K. Sung, *Phys. Chem. Chem. Phys.*, 2023, **25**, 14627–14634.
80 K. D. Warner, M. C. Chen, W. Song, R. L. Strack, A. Thorn, S. R. Jaffrey and A. R. Ferre-D'Amare, *Nat. Struct. Mol. Biol.*, 2014, **21**, 658–663.
81 M. Mieczkowski, C. Steinmetzger, I. Bessi, A. K. Lenz, A. Schmiedel, M. Holzapfel, C. Lambert, V. Pena and C. Hobartner, *Nat. Commun.*, 2021, **12**, 3549.
82 L. F. M. Passalacqua, M. T. Banco, J. D. Moon, X. Li, S. R. Jaffrey and A. R. Ferre-D'Amare, *Nature*, 2023, **618**, 1078–1084.
83 A. Singh, S. Karmakar, I. M. Abraham, D. Rambabu, D. Dave, R. Manjithaya and T. K. Maji, *Inorg. Chem.*, 2020, **59**, 8251–8258.
84 W. Guo-jian, Z. Qi, D. Hong-ping, W. Da-li, Z. Xin-yuan and Y. De-yue, *Acta Polym. Sin.*, 2013, **013**, 660–667.
85 E. A. Dolgopolova, T. M. Moore, W. B. Fellows, M. D. Smith and N. B. Shustova, *Dalton Trans.*, 2016, **45**, 9884–9891.
86 D. E. Williams, E. A. Dolgopolova, P. J. Pellechia, A. Palukoshka, T. J. Wilson, R. Tan, J. M. Maier, A. B. Greytak, M. D. Smith, J. A. Krause and N. B. Shustova, *J. Am. Chem. Soc.*, 2015, **137**, 2223–2226.
87 J. Riedl, P. Menova, R. Pohl, P. Orsag, M. Fojta and M. Hocek, *J. Org. Chem.*, 2012, **77**, 8287–8293.
88 T. Kanamori, A. Takamura, N. Tago, Y. Masaki, A. Ohkubo, M. Sekine and K. Seio, *Org. Biomol. Chem.*, 2017, **15**, 1190–1197.
89 C. H. Wolstenholme, H. Hu, S. Ye, B. E. Funk, D. Jain, C. H. Hsiung, G. Ning, Y. Liu, X. Li and X. Zhang, *J. Am. Chem. Soc.*, 2020, **142**, 17515–17523.
90 Q. Gan, G. Xu, X. Deng, M. Liu, Y. Deng, W. Lu, Y. Ruan, C. Fu and Y. Yu, *J. Colloid Interface Sci.*, 2024, **654**, 698–708.
91 H. Guo, M. Fan, Z. Li, W. Tang and X. Duan, *Anal. Methods*, 2018, **10**, 5629–5633.
92 S. L. Tou, G. J. Huang, P. C. Chen, H. T. Chang, J. Y. Tsai and J. S. Yang, *Chem. Commun.*, 2014, **50**, 620–622.
93 S. K. Dey, G. S. Filonov, A. O. Olarerin-George, B. T. Jackson, L. W. S. Finley and S. R. Jaffrey, *Nat. Chem. Biol.*, 2022, **18**, 180–190.
94 N. Ruan, X. Yu, H. Li, Y. Wang and C. Huang, *Chem. – Asian J.*, 2022, **17**, e202200383.
95 J. S. Paige, K. Y. Wu and S. R. Jaffrey, *Science*, 2011, **333**, 642–646.
96 W. Song, G. S. Filonov, H. Kim, M. Hirsch, X. Li, J. D. Moon and S. R. Jaffrey, *Nat. Chem. Biol.*, 2017, **13**, 1187–1194.
97 X. Li, H. Kim, J. L. Litke, J. Wu and S. R. Jaffrey, *Angew. Chem., Int. Ed.*, 2020, **59**, 4511–4518.
98 J. N. Han, C. Zhong, M. Ge, S. Kuang and Z. Nie, *Chem. Sci.*, 2023, **14**, 4538–4548.
99 G. Feng, C. Luo, H. Yi, L. Yuan, B. Lin, X. Luo, X. Hu, H. Wang, C. Lei, Z. Nie and S. Yao, *Nucleic Acids Res.*, 2017, **45**, 10380–10392.
100 B. S. VarnBuhler, J. Moon, S. K. Dey, J. Wu and S. R. Jaffrey, *ACS Chem. Biol.*, 2022, **17**, 840–853.
101 F. Würthner, *Angew. Chem., Int. Ed.*, 2020, **59**, 14192–14196.
102 J. Gierschner, J. Shi, B. Milián-Medina, D. Roca-Sanjuán, S. Varghese and S. Park, *Adv. Opt. Mater.*, 2021, **9**, 2002251.
103 J. Dong, K. M. Solntsev and L. M. Tolbert, *J. Am. Chem. Soc.*, 2009, **131**, 662–670.
104 S. Fery-Forgues, S. Veesler, W. B. Fellows, L. M. Tolbert and K. M. Solntsev, *Langmuir*, 2013, **29**, 14718–14727.
105 G. Xu, X. Yao, X. Deng, C. Fu, W. Li, M. Liu, W. Lu, Y. Ruan, T. Chen and Y. Yu, *J. Mol. Struct.*, 2025, **1322**, 140517.
106 B. P. Mali, S. R. Dash, M. Annadhasan, A. Biswas, K. Manoj, K. Vanka and R. G. Gonnade, *Cryst. Growth Des.*, 2023, **23**, 5052–5065.
107 N. B. Dabke, Y. Raut, B. P. Mali, R. Pandya, K. Vanka, K. Manoj and R. G. Gonnade, *J. Mater. Chem. C*, 2024, **12**, 8368–8379.
108 V. Virole, N. Dabke, S. Verma, A. Kumar, R. Pandya, S. Husale, K. Vanka, R. Gonnade and R. Kanawade, *Nanoscale*, 2025, **17**, 8614–8623.
109 A. Singh, D. Samanta, M. Boro and T. K. Maji, *Chem. Commun.*, 2019, **55**, 2837–2840.
110 F. A. Rahimi, A. Singh, R. Jena, A. Dey and T. K. Maji, *ACS Appl. Mater. Interfaces*, 2024, **16**, 43171–43179.
111 G. Anjum, A. Kumar, G. Ramanathan and J. N. Moorthy, *Mater. Adv.*, 2024, **5**, 9279–9291.
112 Y. Zheng, G. Li, H. Deng, Y. Su, J. Liu and X. Zhu, *Polym. Chem.*, 2014, **5**, 2521–2529.
113 W. Fan, H. Deng, L. Zhu, C. Tu, Y. Su, L. Shi, J. Yang, L. Zhou, L. Xu and X. Zhu, *Biomater. Sci.*, 2019, **7**, 2421–2429.
114 H. Deng, Q. Zhu, D. Wang, C. Tu, B. Zhu and X. Zhu, *Polym. Chem.*, 2012, **3**, 1975–1977.

115 D. Hong-ping, Q. Zhu, W. Da-li, Z. Bang-shang and Z. Xin-yuan, *Acta Polym. Sin.*, 2012, **012**, 1136–1142.
116 H. Deng, Y. Su, M. Hu, X. Jin, L. He, Y. Pang, R. Dong and X. Zhu, *Macromolecules*, 2015, **48**, 5969–5979.
117 Y. Ren and C. Huang, *J. Mater. Chem. B*, 2025, **13**, 2327–2334.
118 Q. Zhou, F. Wu, M. Wu, Y. Tian and Z. Niu, *Chem. Commun.*, 2015, **51**, 15122–151224.
119 A. Baldridge, S. R. Samanta, N. Jayaraj, V. Ramamurthy and L. M. Tolbert, *J. Am. Chem. Soc.*, 2010, **132**, 1498–1499.
120 A. Baldridge, A. Amador and L. M. Tolbert, *Langmuir*, 2011, **27**, 3271–3274.
121 N. Ruan, Q. Qiu, X. Wei, J. Liu, L. Wu, N. Jia, C. Huang and T. D. James, *J. Am. Chem. Soc.*, 2024, **146**, 2072–2079.
122 H. Jin, D. Shen, B. Jing, Z. Zhang, Z. Wang, R. Sun, H. Zhang, J. Sun, H. Lyu, Y. Liu and L. Wang, *Anal. Chim. Acta*, 2023, **1278**, 341704.
123 S. Ye, C. H. Hsiung, Y. Tang and X. Zhang, *Acc. Chem. Res.*, 2022, **55**, 381–390.
124 A. Belousov, I. Maslov, P. Orekhov, P. Khorn, P. Kuzmichev, N. Baleeva, V. Motov, A. Bogorodskiy, S. Krasnova, K. Mineev, D. Zinchenko, E. Zernii, V. Ivanovich, S. Permyakov, J. Hofkens, J. Hendrix, V. Cherezov, T. Gensch, A. Mishin, M. Baranov, A. Mishin and V. Borshchevskiy, *iScience*, 2024, **27**, 110466.
125 J. Ouellet, *Front. Chem.*, 2016, **4**, 29.
126 R. L. Strack, M. D. Disney and S. R. Jaffrey, *Nat. Methods*, 2013, **10**, 1219–1224.
127 W. Song, R. L. Strack, N. Svensen and S. R. Jaffrey, *J. Am. Chem. Soc.*, 2014, **136**, 1198–1201.
128 N. Kikuchi and D. M. Kolpashchikov, *ChemBioChem*, 2016, **17**, 1589–1592.
129 G. S. Filonov, J. D. Moon, N. Svensen and S. R. Jaffrey, *J. Am. Chem. Soc.*, 2014, **136**, 16299–16308.
130 K. Huang, Q. Song, M. Fang, D. Yao, X. Shen, X. Xu, X. Chen, L. Zhu, Y. Yang and A. Ren, *Nat. Chem. Biol.*, 2024, **20**, 1453–1460.
131 L. Jiang, X. Xie, N. Su, D. Zhang, X. Chen, X. Xu, B. Zhang, K. Huang, J. Yu, M. Fang, B. Bao, F. Zuo, L. Yang, R. Zhang, H. Li, X. Huang, Z. Chen, Q. Zeng, R. Liu, Q. Lin, Y. Zhao, A. Ren, L. Zhu and Y. Yang, *Nat. Methods*, 2023, **20**, 1563–1572.
132 L. Cai, H. Li, X. Yu, L. Wu, X. Wei, T. D. James and C. Huang, *ACS Appl. Bio Mater.*, 2021, **4**, 2128–2134.
133 M. Zhang, J. Liu, X. Yuan, Y. Wen and C. Huang, *Anal. Bioanal. Chem.*, 2025, **417**, 6221–6229.
134 S. N. Hassan and F. Ahmad, *Exp. Oncol.*, 2024, **46**, 174–178.
135 S. Tunçer, R. Gurbanov, I. Sheraj, E. Solel, O. Esenturk and S. Banerjee, *Sci. Rep.*, 2018, **8**, 14828.
136 M. Verheijen, M. Lienhard, Y. Schrooders, O. Clayton, R. Nudischer, S. Boerno, B. Timmermann, N. Selevsek, R. Schlapbach, H. Gmuender, S. Gotta, J. Geraedts, R. Herwig, J. Kleinjans and F. Caiment, *Sci. Rep.*, 2019, **9**, 4641.
137 C. L. Walker, K. A. Lukyanov, I. V. Yampolsky, A. S. Mishin, A. S. Bommarius, A. M. Duraj-Thatte, B. Azizi, L. M. Tolbert and K. M. Solntsev, *Curr. Opin. Chem. Biol.*, 2015, **27**, 64–74.
138 W. Li, W. Feng, B. Liu and Y. Qian, *J. Photochem. Photobiol., A*, 2023, **445**, 115045.
139 C. Steinmetzger, N. Palanisamy, K. R. Gore and C. Hobartner, *Chemistry*, 2019, **25**, 1931–1935.
140 D. Grabarek and T. Andruniów, *Int. J. Quantum Chem.*, 2019, **120**, e26086.
141 A. G. Tebo, B. Moeyaert, M. Thauvin, I. Carlon-Andres, D. Boken, M. Volovitch, S. Padilla-Parra, P. Dedecker, S. Vriz and A. Gautier, *Nat. Chem. Biol.*, 2021, **17**, 30–38.
142 B. Perillo, M. Di Donato, A. Pezone, E. Di Zazzo, P. Giovannelli, G. Galasso, G. Castoria and A. Migliaccio, *Exp. Mol. Med.*, 2020, **52**, 192–203.
143 M. E. Bulina, K. A. Lukyanov, O. V. Britanova, D. Onichtchouk, S. Lukyanov and D. M. Chudakov, *Nat. Protoc.*, 2006, **1**, 947–953.